UNIVERSITÀ DEGLI STUDI DI GENOVA
Scuola di Dottorato in Ingegneria dei Sistemi
Indirizzo Monitoraggio dei sistemi
XXIX Ciclo

High-resolution hydro-meteorological modeling of extreme weather events over complex orography areas: applications of WRF and WRF-Hydro model configurations.

Francesca Viterbo

Internal supervisor: Ing. Antonio Parodi Ph.D.
External supervisor: Dott. Jost Von Hardenberg Ph.D.
Coordinatore del Dottorato: Prof. Simona Sacone Ph.D.

Anno accademico 2016-2017

For anyone who trusts an idea
and just will not stop tilting at windmills
to make it come true.

Contents

Introduction

The main aim of this thesis is to investigate the complexity of modeling extreme hydrometeorological events in complex orography areas, starting from the atmospheric processes to terrestrial hydrology at different spatial and temporal scales. This work intends also to compare the classical stand alone meteorological approach with a fully coupled representation of the water cycle, and to explore possible improvements in terms of precipitation predictability of extreme flooding events in both of these configurations.

The WRF meteorological model has been used several times as a dynamical downscaler to understand the physical processes responsible of extreme rainfall events (Gallus Jr and Bresch (2006), Heikkilä et al. (2011), Gao et al. (2012), Fiori et al. (2014), Viterbo et al. (2016), etc.). Non-hydrostatic models have shown substantial success in simulating realistic heavy precipitation events (Stein et al. (2000); Richard et al. (2003), Asencio et al. (2003)), even if intrinsic predictability limits are part of the problem as a result of the non-linearity and instability of the atmosphere dynamics, together with the lack of a precise knowledge of the atmospheric state at any time and location. High-resolution meteorological models have still to deal with the limits of computational costs of simulations, observational data quality and availability, parameterization of the subgrid processes, resolution, physical description, etc.

Historically, the atmosphere and the terrestrial hydrologic cycles have not been well integrated in terms of coupled modeling systems. In the past precipitation and runoff relationship has been maintained separate, with a sort of one way cause-effect relationship, relating each other. Recently the need for improving hydro-meteorological predictions for flood, droughts and water resources has become more critical and has promoted a fully two-way coupled atmospheric-hydrologic approach. Fully coupled high-resolution models, such as the coupled WRF/WRF-Hydro system, are new generation tools designed to link multi scale processes of the atmosphere and terrestrial hydrology and to perform coupled and uncoupled multi-physics simulation at wide range of spatial and temporal scales. The improved process representation of lateral redistribution and infiltration runoff and exfiltration processes provide a more complete depiction of terrestrial hydrologic states and fluxes which influence land-atmosphere energy exchanges. In this framework the use of WRF-Hydro fully coupled model is compared to the classical WRF stand alone meteorological approach to investigate the situations in which the fully coupled configuration may provide tangible improvement in the study of precipitation events.

In this work, I develop a series of application of the WRF Meteorological model

and of WRF-Hydro in the complex orography areas to investigate: 1) the capability of each model suite to describe the physical processes leading to severe rainfall in complex topography 2) the sensitivity of each model configuration to the choice of different parameterizations and the importance of a correct model calibration for both atmospheric and hydrological needs 3) the possible improvement in predictability if we compare WRF stand alone and WRF-Hydro model application 4) whether it is more relevant a better description of the dynamics (higher resolutions, correct choice of parameterizations etc.) or a better representation of the physical processes (meteorological only approach vs. fully coupled hydro-meteorological WRF-Hydro simulations) in the representation of extreme hydrometeorological events at the event and seasonal temporal scales.

I have applied the WRF and WRF-Hydro model to two case studies in Northern Pakistan and in the Tiber river basin in central Italy. In the first part of the work the predictability of the WRF model, operated at the very fine resolution of 3.5 km has been explored in reproducing the 2010 Pakistan flood over complex topography of the Hindu-Kush-Himalaya-Karakorum (HKKH) region. The model results are compared with Tropical Rainfall Measuring Mission (TRMM) rainfall estimates, the available ground measurements, and radar observations from the CloudSat mission. In particular, the sensitivity of the WRF simulations to the use of different convective closures (explicit and Kain-Fritsch), microphysical parameterizations (WRF single-moment 6-class microphysics scheme and Thompson) and different initial conditions associated with a different initialization day, is also examined. This work has developed as natural continuation of my master degree thesis and it has successively been shaped in a form of a proper independent research topic, enlarging the discussion to the ability of WRF in reproducing the time-scale interaction of precipitation processes from large to small scales. On a first instance, I have validated the model results with the available observation of TRMM and raingauges using classical statistical scores derived from the traditional calculation of percentiles (60th and 95th), root-mean-square error (RMSE), mean bias (MB). I have further added innovative methods such as MODE object based verification tool (Davis et al. (2006a), Davis et al. (2006b) and Brown et al. (2007)) and I have used of the new-generation Distributed Simulation and Stimulation System NASA Earth Observing System Simulators Suite radar simulator (Tanelli et al. (2002) and Tanelli et al. (2011, 2012). These instruments allow a more accurate and extensive investigation of the mesoscale processes in terms of precipitation patterns and of the interaction with the complex orography. In addition to that, I also performed small variation of the initial condition and boundary conditions to perform a sensitivity analysis to the processes that characterized Pakistan 2010 flood producing storm. The results indicates that a careful choice of parameterization scheme and initialization day must always be adopted, because these factors can significantly affect the simulation. Configurations that exhibit small differences at synoptic scales start to produce very different precipitation amounts, patterns, and circulations, especially over mountain terrain, at mesoscale. The reliability of the large-scale fields used for initialization and boundary conditions remains an essential ingredient of the simulation. Errors in the large-scale fields can be propagated, or even amplified, in the outputs of high-resolution simulations. Inter-scale phenomena

and orography interaction are thus predominant features in studying these particular processes over complex orography areas such as HKKH. In this experimental case I had the occasion to analyze the sensitivity of the atmospheric model to different parameterizations. Even if the results gained are encouraging, they are still strongly conditioned by the resolution, the choice of model physical parameterizations and limits in computational resources. Finally, small displacement in precipitation in mountain areas can produce very different results in hydrological simulation. For this reason I have considered the terrestrial hydrology to the study of physical processes, trying to understand if a better representation of the physical processes can help in improving the simulation of extreme hydrometeorlogical events.

In the second model study, I consider the comparison of a WRF stand alone approach with a WRF-Hydro fully coupled application at the seasonal scale (two years long simulations), over the Tiber river basin in central Italy.

Meteorological and hydrological approaches are strongly related but they deal with different time and spatial scales and different model approaches. In the first part of the work, I have performed two different one-year long experiments at 4 km grid resolution in stand alone WRF configuration with one single-moment and one double-moment mycrophisics schemes (Thompson and WSM6 microphysics) in order to choose a reference setup of the WRF atmospheric model for the study region and corresponding extreme hydrometeorological events at the temporal scales of interest. In the second step of the study I calibrate the hydrological model at seasonal scale with a perfect forcing provided by observations and analysis data instead of model variables. Finally, only when the both the atmospheric and the hydrological models have been properly calibrated and validated, I perform the WRF-Hydro fully-coupled run as third and final step. The simulations of the fully coupled hydrometeorological experiment, reveal more reactive soil moisture dynamics and higher contribution of evapotranspiration to the water balance with consequent minor production of the surface runoff and higher underground runoff. Even if the feedback on the occurrence of extreme precipitation events is modest, the overall simulations show a good accordance with the available observation and represent an added value in the study of the water cycle. With only one simulation it is possible to simulate precipitation events and the terrestrial hydrology response in terms of channel network, water resources and distributed variables such as soil moisture and runoff at high resolution.

The structure of this thesis is organized as follows. Chapter 1 provides a brief review on the current scientific knowledge regarding the problem of predictability of extreme hydrometeorological events in complex orography areas and the related hydrometeorological modeling challenges. Chapter 2 describes in detail the WRF and WRF-Hydro models and their calibration and validation strategies. In chapter 3 I apply the WRF stand alone as a dynamical downscaler to study the tragic event of 2010 Pakistan flood and I explore the sensitivity of the model to different configurations. Chapter 4 describes the WRF and WRF-Hydro fully coupled experiment over Tiber river basin. In the first part of the chapter I describe the role of meteorological and hydrological calibration in the preparation of the fully coupled WRF-Hydro experiment. In the last part I compare

the two different approaches and I investigate the possible improvement in precipitation predictability when the soil-precipitation feedbacks act over a seasonal simulation. Finally, the final conclusions and possible future developments are discussed in the last chapter.

Chapter 1

Predictability of Extreme hydrometeorological events over complex orography areas

1.1 Introduction

There is a strong necessity of high-resolution atmospheric modeling in mountain region where the accurate prediction of timing and amount of precipitation become crucial for hydrological purposes. Even if the occurrence of an intense event can be predicted relatively in advance from the large scale, the small scales and the orographic component can deeply influence the evolution of the phenomena in terms of precipitation triggering and in terms of rainfall-runoff response. In this chapter the concepts of extreme event and predictability (section 1.2 and section 1.4) are introduced and the main challenges related to modeling extreme events in complex orography areas are addressed (section 1.3). The differences between typical meteorological and hydrological scales are introduced in section 1.5). A theoretical overview over the atmospheric and hydrological modeling is given in section 1.6 and section 1.7. Finally, the key role of soil-atmosphere interactions and land surface modeling is explained in section 1.8.

1.2 Extreme hydrometeorological events

According to the definition of the Intergoventamental Panel on Climate Change (IPCC), an extreme weather or climate event is defined as "the occurrence of a value of a weather or climate variable above (or below) a thereshold value near the upper (or lower) ends of the range of observed values of the variable" (Field, 2012). In some cases an extreme event is not only caused by a variation in a single atmospheric variable, but is is a result of a specific condition of several variables, surface properties or states (Field, 2012). Extreme weather events include a wide range of events, from severe events like heavy precipitation and flash flooding to severe cyclogeneses, from heat waves and droughts to tornadoes, and

hurricanes. Many of these extreme events are a results of natural variability like inter-annual phenomena such as El Nino, or natural decadal and multi-decadal variations in climate. Nevertheless, man-induced climate change is likely to increases the frequency and intensity of extreme weather events and their impacts over many areas of the globe (Field, 2012). According to Munich Reinsurance Company report, global losses due to adverse natural events were estimated at 4.2 trillion between 1980 and 2014. During this period, this losses have raised from $50 billion a year in the 1980s to nearly $200 billion a year in the last decade. Almost 75% of such losses are attributable to extreme weather events. Agenda 21 is the United Nations action plan for the 21st Century on sustainable development, produced in 1992 at the Earth Summit (UN Conference on Environment and Development) in Rio de Janeiro. An intere chapter of the Agenda 21 is dedicated to mountain regions, since they represent a source of fresh water, energy, minerals, forest and agricultural products and areas of recreation and they are expected to be one of the most sensible environments to the effects of climate change. This is particularly important if we consider that resources from mountain areas indirectly provide sustenance for over half of the global populations and 40% of global population lives in the watersheds of rivers originating in the planet's different mountain ranges (Summit, 1992). Consequences for river runoff are likely to affect not only the watersheds within the mountains themselves, but also in the lowland regions that are heavily dependent on this mountain resource.

1.3 Complex orography areas

Orographically-enhanced precipitation may represent a significant fraction of annual or seasonal rainfall in a particular mountain region. The presence of topographic barriers can act as triggering mechanism that enhance precipitation processes (National Research Council (US). Committee to Assess NEXRAD Flash Flood Forecasting Capabilities at Sulphur Mountain, California, 2005). A synoptically forced flow over a topographic barrier can deeply interact with the storm dynamics and may lead to persistent and orographically enhanced storm systems with an anomalous increased intensity and duration in time (Smith (1979); Bruintjes et al. (1994); Buzzi et al. (1998); Rotunno and Ferretti (2001); Medina and Houze (2003)). In some cases the inter-scale interaction between large and small scales became even stronger, since the precipitation systems are fed by low level jets of near saturated air, increasing warm rain processes (Maddox et al. (1978); Caracena et al. (1979); Barros and Lettenmaier (1994); Reinking and Boatman (1986); Kelsch et al. (2001)). In addition to that, the flooding impact can be increased in some cases, when the phenomena is concurrent with melting snow dynamics (Barros and Kuligowski, 1998). The complex dynamic interactions of mountain regions has been investigated in many complex topography areas of the world and still represent a challenging target in terms of predictability (see Houze Jr et al. (1976), Hobbs and Persson (1982), Barros and Lettenmaier (1994), Neiman et al. (2002), Neiman et al. (2004), Ralph et al. (2006), Webster et al. (2011)). In mountain areas small horizontal gradients corresponds to great variations in terms of precipitation variability influenced by steepness, altitude, temperature and typical small scale ridges and valley phenomena

Anders et al. (2006). The presence of a mountain range is a potential source of severe uncertainty in numerical simulations and forecasts, and cannot be properly captured by coarse grid spacing General Circulation Models (GCMs). ECMWF and GFS products are available at grid spacing between 0.5°and 0.75°and, even if the precipitation forecast was predictable with reasonably good skills, convective features of the event and orographic characteristics act on scales finer than the GCM pixel resolution and could not be appreciated (Rasmussen et al. (2014), Viterbo et al. (2016)).

In such applications also atmospheric model verification or model initialization it's challenging: because of the inaccessibility of mountain regions, observation are scarce and strongly biased. Rain gauge stations are mainly located in valley floors (Fowler and Archer, 2006) and, for this reason, regions above 5 km still remain poorly monitored (Palazzi et al., 2013a). The available gauge observations are scarce and are largely biased by altitude, mainly because of technical reasons such as the difficulty to measure the snow water equivalent depth and the deflection of precipitation by winds (see, e.g., Winiger et al. (2005), Anders et al. (2006); Barros et al. (2006)). On the other hand, remote observations provide spatially complete coverage of precipitation estimates, but local conditions cannot be incorporated in the sensor algorithm, with potentially large errors within each point of the grid space (Andermann et al., 2011). Uncertainty in the precipitation estimates in terms of intensity and pattern reflects in inaccurancy in hydrologic response: a small displacement of the forecasted precipitation fields can produce very different effects in terms of runoff over mountain catchments. Mountain catchments are really small in they initial part. A displacement of a precipitation field of few kilometers can overpass the catchment divide and displace the precipitation input from one catchments to a completely different one. In addition to that, steep orography can funnel the intense runoff from severe rain events into river basins and increase the chance of a flood to happen. The flooding event not only depends on the amount of rain, but it is also strongly conditioned by the hydrologic characteristics of the single watershed, such as soil saturation and permeability, vegetation state, slope, urbanization etc (National Research Council (US). Committee to Assess NEXRAD Flash Flood Forecasting Capabilities at Sulphur Mountain, California, 2005).

1.4 The concept of predictability

The concept of predictability is a necessary question to be introduced any time we are speaking about atmospheric modelling and their related impacts in terms of hydrological response. This topic started to be addressed by Lorenz (1969a) (or even before by Thompson (1957)), regarding the uncertanty related to the predictability of flow which possesses many scales of motion. Atmospheric modelling try to use the equations of fluid dynamics to predict future states of the atmosphere (as described in section 1.6) but they have to deal with some intrinsic limit of their predictive ability. The problem lies on the fact that we can incorporate into the models equations that more closely describe the real atmospheric states, but they still represent a partial and imperfectly theoretical description of reality. In addition to that, we have to take into account that the initial

state cannot be described with sufficient accuracy due to inadeguate observational data, and, finally, the numerical methods and computers yield only approximate solutions of the equations that are used. Two of this limits (the first and the latter) are constrained by technical and scientific limits of numerical weather prediction. In an hypothetical future, equation can became more accurate in the description of the dynamic, computing science can progress in the direction of methods of approximation and computer power, as well. The accuracy of the prediction can grow to became nearly perfect, except for the fact the we still have errors related to initial conditions. Even if we have the most accurate instrument of measure, there will always be, at least in principle, small-scale phenomena that we do not observe (Somerville, 1987). Because of the features of turbulent fluids in general, unresolved little eddies and instabilities will grow in time together with the forecast errors. The forecast skills evolve till they reach the asymptotic state of "worthless prediction", in which two initial resemblant atmospheric states decrease their forecast skills till at some time the resemblance will be not better than two arbitrary atmospheric states randomly chosen (Somerville, 1987). Techniques to estimate the precipitation predictability has been studied in Lorenz (1969b), Thompson (1957), Davis (1978), Zhang et al. (2006), Clark et al. (2009) and in many other studies in literature. Any forecast loose skills because of intrinsic instability of the atmosphere itself. Small errors grows can double in about two days, faster than larger errors (Fig. 1.1). The maximum deterministic range of forecast is defined as the time which the errors have reached their asymptotic value, till a maximum performance value of two weeks. The actual achieved forecast skills are still far from the theoretical concept of predictability.

Apart from the atmospheric modelling, also hydrologic modelling posses major sources of uncertainty derived from structural errors, parameter errors, and data errors (Wagener and Gupta, 2005). Hydrological models are derived from assumptions and simplifications and results in an inevitably imperfect approximations to the complex reality. Structure errors can also arise from the mathematical implementation that transforms a conceptual model into a numerical model (Neuman, 2003). Model parameterization pretends to represent aggregated spatially and temporally heterogeneous properties of the real system. Moreover, hydrological data are not often easily measurable, and generally estimated indirectly by prior knowledge or model calibration, with consequent introduction of errors and uncertainties. Model inputs and initial conditions can be estimated from observations and generate uncertanties in hydrologic preditions (Clark and Slater, 2006). A data error is also related to measurement errors. This error can be given due to imperfect measurement devices that do not accurately record the variables they are designed to measure or due to representativeness error due to scale incompatibility between the variable measured by a device and the corresponding model variable.

All this kind of errors collectively lead to uncertainties in hydrologic predictions of model outputs and states. Structural errors are generally the most poorly understood and the most difficult to cope with; nevertheless, their impacts on hydrologic predictions can be far more detrimental than those of parameter errors and data errors (Carrera and Neuman (1986); Abramowitz et al. (2006)). As of today, our understanding of hydrologic uncertainty is still far from complete and there is much room for further efforts in search

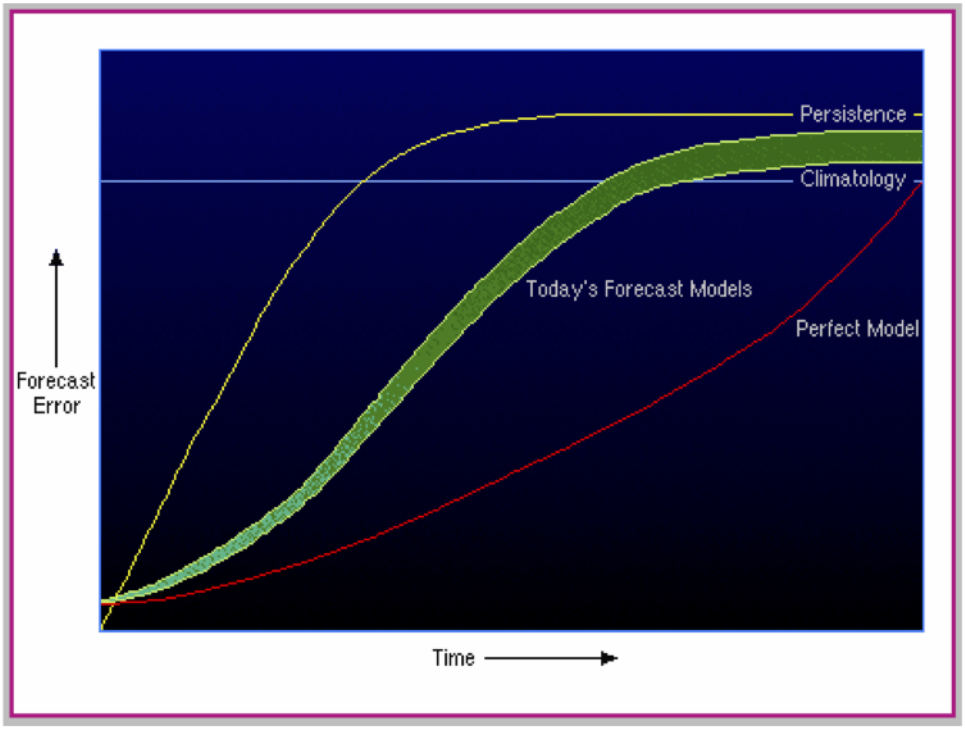

Figure 1.1: Forecast error growth and predictability (Source: COMET UCAR Program).

of cohesive, systematic means to approach this. Proper consideration of uncertainty in hydrologic predictions is essential for purposes of both research and operational modeling (Wagener and Gupta, 2005).

Obviously, an adequate understanding of all the different uncertainty sources and the relationships between them is a fundamental aspect to be taken into consideration, especially if we are speaking about a system that incorporates both atmospheric and hydrologically uncertainties (fully coupled hydro-meteorological experiments). In these cases uncertainty quantification is difficult to achieve and reduced in a meaningful way. Different uncertainty sources may introduce significantly different error characteristics that require to be solved using different techniques. Missing important uncertainty sources may lead to misleading uncertainty predictions in the hydrologic outputs. It is also very important to distinguish modeling uncertainty from predictive uncertainty: while modeling uncertainty comes mainly from the imperfect fit to the truth of the past, predictive uncertainty can also arise from extrapolation errors or temporal prediction errors due to the fact that the future typically does not look exactly like the past (Morgan et al. (1992); Krupnick et al. (2006)]). In other words, predictive uncertainty is related to, but not necessarily equivalent to, modeling uncertainty; and reduction in modeling uncertainty does not necessarily lead to enhanced predictability of the model under changing conditions.

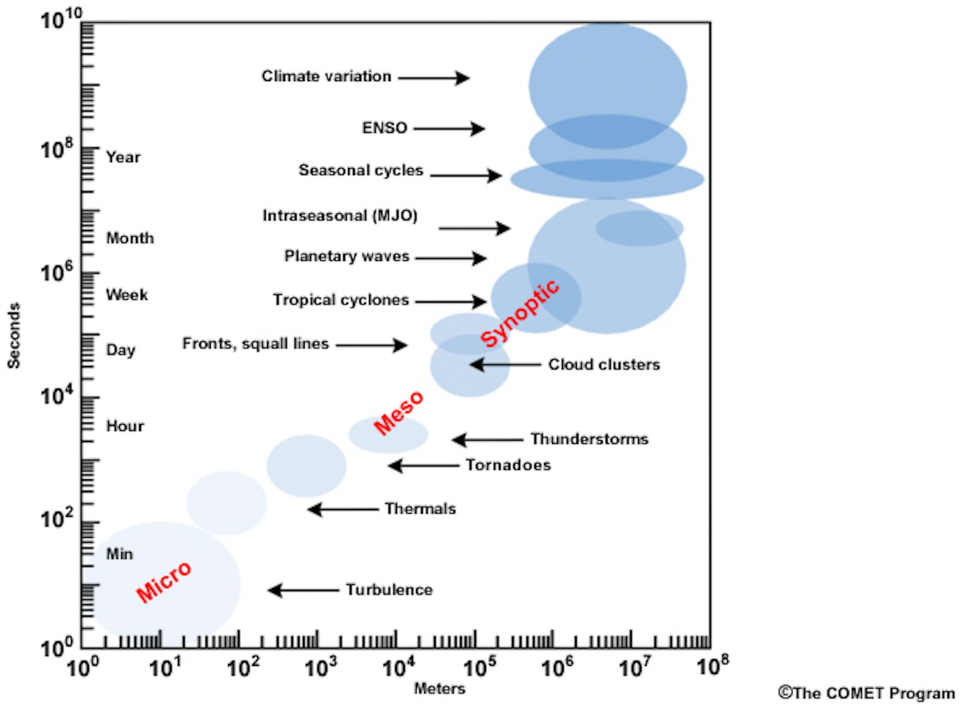

Figure 1.2: Meteorological typical spatial and temporal scales (Source: COMET UCAR Program).

1.5 Meteorological and hydrological scale interactions

Most of the meteorological processes that can contribute to flooding events happen at the synoptic scale and mesoscale. The synoptic scale is defined as meteorological features of scales in excess of 2000 km and includes the well-understood features of troughs, ridges, highs, lows and frontal boundaries, that normally persist from days to weeks (Holton and Hakim, 2012). Mesoscale meteorology deals with smaller weather features included from 2000 km to 2 km (Fig. 1.2). Since this scale included very different phenomena like mesoscale convective systems (MCS), tropical cyclones, thunderstorm convection, it is further differentiated in mesoscale α, mesoscale β, mesoscale γ, with characteristic time scales from days (mesoscale α) to few hours (mesoscale γ) (Orlanski, 1975).

In mesoscale meteorology the geostrophic approximation is not reliable anymore. The hypothesis of geostrophic equilibrium exists when there is a balance between the Coriolis and horizontal pressure forces. The Rossby dimensional number, Ro, (equation 1.1) defines this relationship between the Coriolis forces and horizontal pressure terms from the Navier-Stokes equations, where U and L are the characteristic velocity and length scale of the process and $f = 2\Omega \sin \phi$ is the Coriolis frequency, where Ω is the angular frequency of planetary rotation and ϕ the latitude.

$$Ro = \frac{U}{Lf} \tag{1.1}$$

When the scale of the phenomena (L) is sufficiently large, Ro became of the order of one or less, meaning that the processes are significantly influenced by the earth's rotation and that geostrophic approximation is not valid anymore. In the extratropical latitudes and free atmosphere, geostrophic balance can give acceptable results for synoptic-scale motions, but not mesoscale.

Hydrostatic equilibrium is defined when the pressure gradient force drawing air upwards, is balanced by the force of gravity pulling air back to the surface. In typical mesoscale phenomena, vertical velocities, driven by processes including buoyancy and topographic effects, can approach or even exceed horizontal velocities (over short distances). As a result, many of the atmospheric processes under the scale of 10 km have non-hydrostatic effects that has to be incorporated in the models. These include surface and atmospheric heat and moisture fluxes, turbulence, convection, evaporation, and condensation.

The choice of the scale we are dealing with includes also some restriction in the grid resolution needed to study the processes we are interested in. According to the linear stability analysis of the Navier-Stokes equations (Kundu et al., 2015), five grid points are required for any numerical model to analyze and resolve the structure of a simple wave-form. Some mesoscale features require model grid-point resolutions of 1-2 km, and sometimes, even if we increase the resolution, many important atmospheric processes can be missed. Finally the effect of topography has to be considered in the description of the meteorology. At a mesoscale, terrain profoundly affects meteorology and sometimes plays a dominant role. At model resolutions of 20 km and less, topographic effects are critical to understanding the local effects on the forecast. Land-sea breezes, venturi effects through mountainous valley, coastal barrier jets, and upslope and downslope winds require high resolution topography to be accurately modeled. The resolutions of the Digital Elevation Model and meteorological model needs to be matched closely for an accurate and meaningful forecast.

For all the aforementioned reasons, the resulting forecasted precipitation has an intrinsic sub-grid uncertainty that has a serious impact on its usefulness for flood prediction purposes.

Additionally, the characteristic scales of the hydrological processes may be much smaller than the ones resolved by the atmospherical models (Fig. 1.3) (Castelli, 1995). The meteorological uncertainty of the forecast can sum to the uncertainty derived from the smaller scales and affect the final uncertainty in the flood prediction (Lanza and Siccardi, 1995)). Hydrologist refers to meteorological uncertainty as an "external-scale" uncertainty, that cannot be reduced improving observational network at the basin scale. This kind of uncertanty increases as far as the atmospheric model focuses on predicting smaller scales typical of hydrology (Ferraris et al., 2002).

In the framework of predictability of extreme weather events and their impacts depends on the contribution of the fine scale processes. Small scales add their non linear

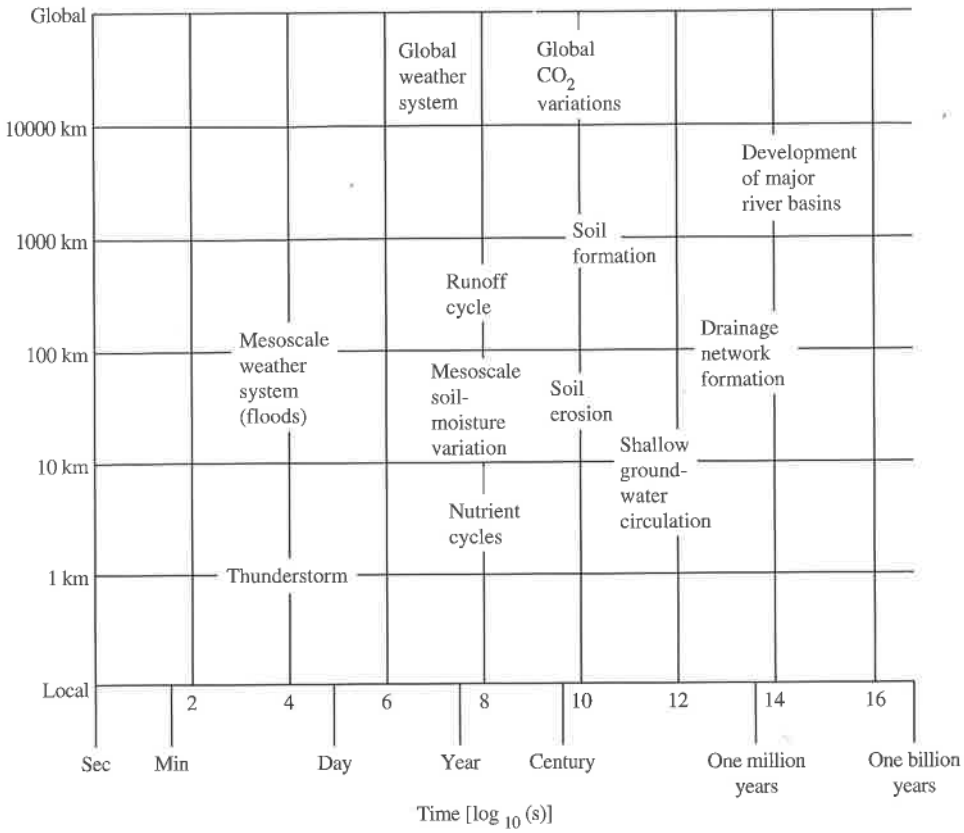

Figure 1.3: Range of space and time of hydrological processes from Dingman (2015)

interaction with large-scale processes, as well as not well defined interactions between oceanic, atmospheric and hydrological processes. High resolution hydro-meteorological models are needed to tackle this fundamental questions.

1.6 Atmospheric modelling

The objective of numerical weather prediction is to predict the future state of the atmosphere from knowledge of its present state by use of numerical approximations to the dynamical equations and boundary conditions.

The atmosphere is considered a fluid governed by a complex interactions of physical laws. It can be described by a system of governing fluidodynamical equations that represents the evolution of its fundamental dynamical and thermodynamical variables. The governing equations can be derived from the principles of the conservation of momentum, the conservation of mass, the conservation of heat (thermodynamic energy), the conservation of water (in terms of mixing ratio or specific humidity) in different forms, and possibly the conservation of other gaseous and aerosol components. A complete description of these equations can be found in all the main text of fluidodynamics, such as Anderson and Wendt (1995), and are illustrated in fig. 1.4. A brief summary of the main terms of these equations is also reported in appendix A.1.

Equation number (5) of the system express the hydrostatic assumption, containing only gravity and vertical-pressure gradients. This approximation is valid at synoptic scale of motions but not valid for most of mesoscale processes description. Mesoscale model are numerical weather prediction model with a sufficiently high horizontal and vertical resolution to forecast mesoscale phenomena (grid spacing typically less than 30 km). This kind of models are able to provide great detail and to accurately represent the intensity of the smaller scales phenomena and obtains superior forecasts in coastal and mountainous region, when compared to large scale phenomena. Non hydrostatic models are generally applied when the length scale of the phenomena is similar to the height scale, such as convective storms, gust fronts, convergence lines, gravity waves, turbulence and tornadoes. They are used in forecast problems that require very high horizontal resolution and cover relatively small domains. The release of buoyancy in the atmosphere and its detailed effects on the development of deep convection is well depicted. An additional forecast equation accounts vertical accelerations and vertical motions directly, rather than determining the vertical motion diagnostically, solely from the horizontal divergence (as an hydrostatic model does). The main disadvantage of a non-hydrostatic model is the longer computation time.

The equations used are non linear partial differential equations which are impossible to solve exactly through analytical methods, with the exception of a few idealized cases. To make the problem mathematically tractable, the reality has to be discretized and simplified using a finite different method. All the parts of the atmospheric model that solve the resolvable scales are called dynamical core. All the representation of the subgrid scale processes are referred as parametrized physical processes (Fig. 1.5).

The finite differences methodology introduces non-physical properties of the model

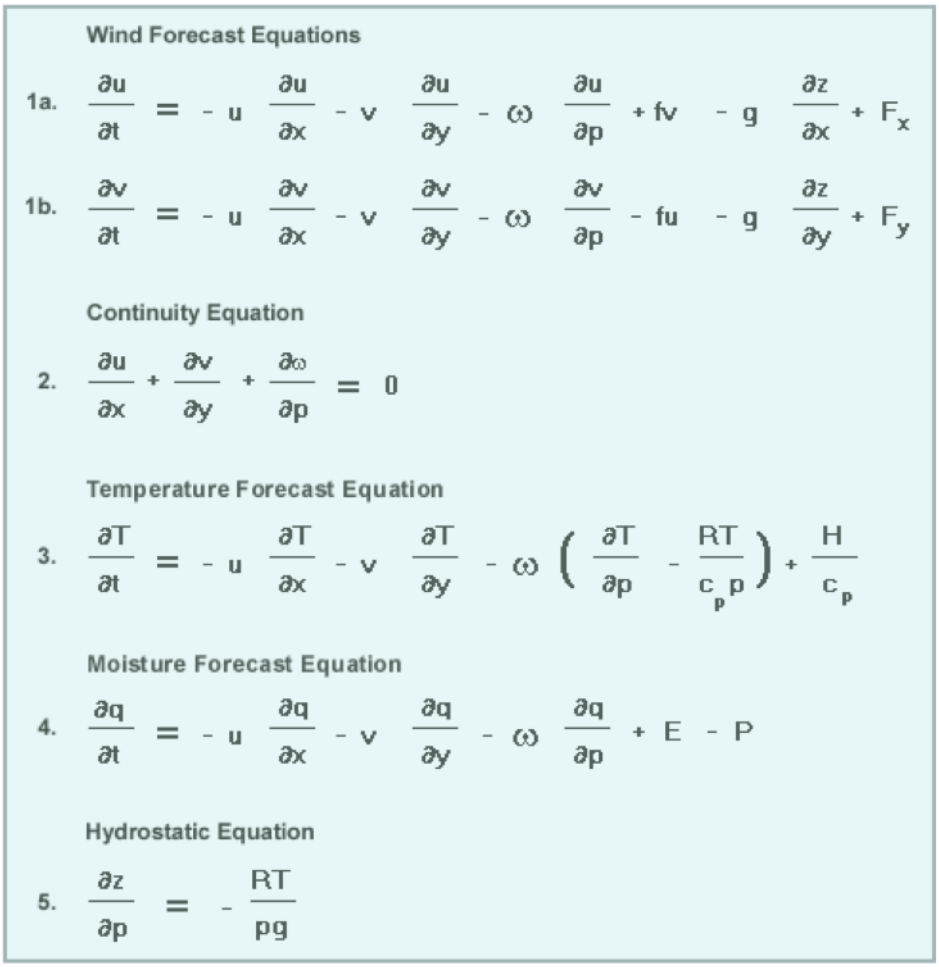

Figure 1.4: Governing equations of numerical weather modelling (Source: COMET UCAR Program). A more detailed of these equations is reported in appendix A.1

solution and introduces stability criteria in model integration that has to match a correct time step. The time step is defined as the rate of change to predict the state of the atmosphere a short time into the future. The equations are then applied to this new atmospheric state to find new rates of change, and these new rates of change predict the atmosphere at a yet further time step into the future. This time stepping is repeated until the solution reaches the desired forecast time. The length of the time step chosen within the model is related to the distance between the points on the computational grid, and is chosen to maintain numerical stability. The main contrition of the time step is given by the Courant number, defined as $\frac{u\Delta t}{\Delta x}$, where u is the horizontal speed of the fastest wave on the grid, Δt is the time step and Δx is the length interval of the resolution of the relevant meteorological process. The Courant number and concepts of numerical stability according to Courant-Friedrichs-Lewy criterion are described in Courant and

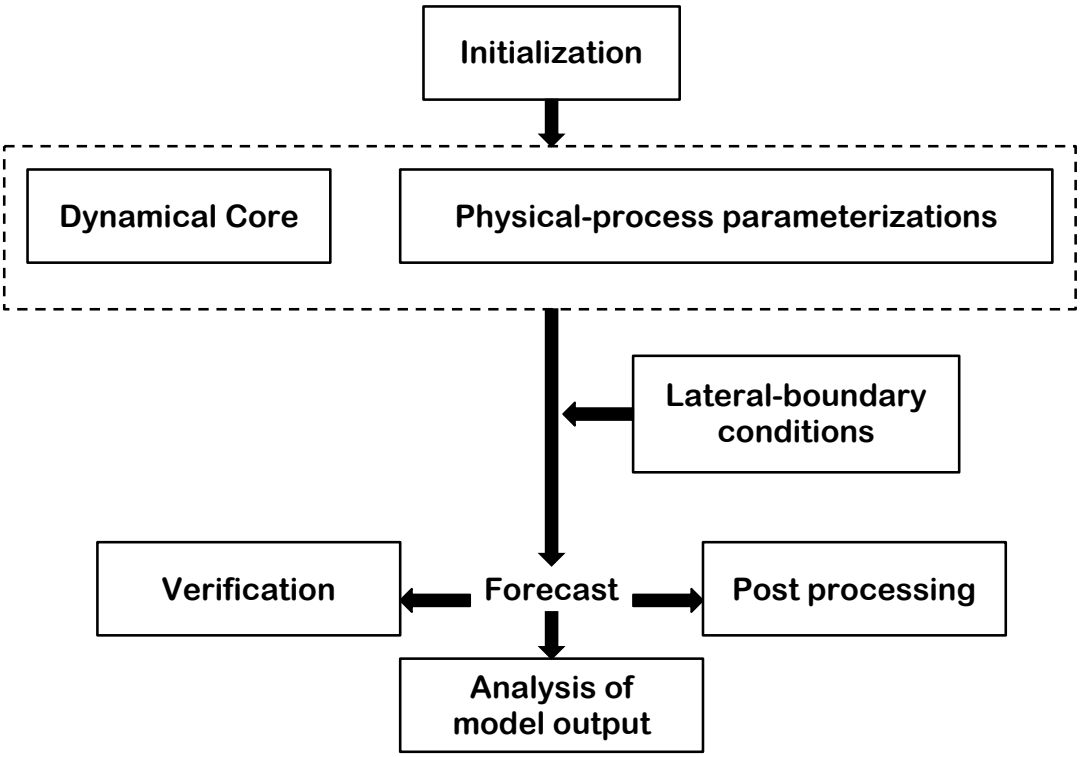

Figure 1.5: Schematic of the typical structure of an atmospherical modelling system. Adapted from Warner (2010)

Lewy (1928), Courant et al. (1943) and Anderson and Wendt (1995).

The area in which the model performs its calculation is called domain. If the domain is extended to all the globe, the model is defined global; otherwise the limited area models cover only specific areas of the planet. Regional models (also known as limited-area models, LAMs) allow for the use of finer grid spacing than global models because the available computational resources are focused on a specific area instead of being spread over the globe. Regional model are usually nested inside the global models. The modern models uses a three dimensional grid to represent the atmosphere on the whole globe.

Grid point models perform their calculations on a fixed array of spatially disconnected grid points both in horizontal and vertical direction. On the horizontal grid the values actually represent an areal average over the grid box. The finer is the resolution of the grid and easier is to describe the finer scale processes, even if the computational cost became more consistent. The greater is the distance between grid points and less likely the model will be able to detect small scale variations in the temperature and moisture fields. Many models have the ability to nest finer grids within a coarse grid resulting in a nested grid with much higher resolution.

On the vertical grid the vertical structure of the atmosphere is described, producing forecasts for the average over an atmospheric layer between the vertical-coordinate surfaces. The vertical representation presents the problem of an eventual interception with terrain and orography: for this reason different terrain following coordinates are used (see Laprise (1992), Janjic (1994), Zängl (2002) and Skamarock et al. (2008) for more informations). Vertical levels are distributed asymmetrically, to gain a better level of detail near the surface and boundary layer. The forecast values of the meteorological variables in each grid cube are derived from the current values within the cube plus those from the surrounding cubes.

Since the system is composed of partial differential equation, boundary conditions and initial conditions are required to let the system be solvable (Fig. 1.5). At the contrary of global models that have no lateral boundaries, limited area models needs lateral boundary conditions that can be provided by interpolation at the boundaries with global models (mostly for operational forecasting needs) or by gridded regional or global analysis of observations. The quality of the simulation is greatly affected by the quality of boundary conditions: errors in forecast from larger-domain models can move and sometimes be amplified in the frame of the limited area model. Accurate information must be provided for all forecast variables and along each model boundary (lateral, top and bottom) in order to solve the forecast equations.

Initialization is the process of entering observation data into the model to generate initial conditions that specify the beginning of the integration. A bad initialization can strongly affect the model outputs. In general, it is reasonable to assume that forecast quality can be no better than that of the initial conditions. In addition to that, inertia gravity waves are created by the model fields in adjusting after the initialization if mass and momentum fields are far out of balance. Finally, if the initial conditions does not contain a realistic representation of realistic vertical motions associated to orography, coastal or mountain-valley circulations, the model requires a certain time (from 12 to 24

hours after the initialization) to spin up these features during the simulation. Most of the initial conditions error may be linked to scarce observational data coverage both in terms of spatial density and temporal frequency, errors in the data for instrument and representativeness biases, errors in quality control, objective analysis, data assimilation and missing variables.

Some meteorological processes are too small-scale or too complex to be explicitly included in numerical weather prediction models. Parameterization is a procedure for representing these processes by relating them to variables on the scales that the model resolves. Weather models need to parameterize cloud microphysics, convective closure and other physical processes such as solar radiation, moist processes, heat exchange, soil, vegetation, water surface and the effects of the terrain. The finite difference equations can only describe scales significantly greater than two grid lengths. Sub-grid scale fluxes of heat, mass and moisture can have considerable impact on the grid-scale flow. Although sub-grid scale processes are not included in a model, parameterization describes their statistical properties in terms of resolved variables.

Once that the model has been run, the model has to be verified in order to evaluate the quality of forecasts (Fig. 1.5). This procedure is necessary for multiple motivations. Verification procedures are useful to understand if the model is reproducing the physical processes of the reality in a correct way. If the model is correctly representing the observation where they are available, there is some confidence that the model can be reliable also when we have no observations. Model and available observation comparison is also useful to asses the model performance, function of the choice of the physical-processes parameterization, vertical and horizontal resolution, lateral boundary conditions, using objective verification statistics. The simulation can be also assessed for different season and meteorological situation in different areas of the world. Model comparison and mode development also imply verification techniques.

In the following chapter 2, the WRF model is introduced and described, as far as the main model reference setup and verification techniques adopted in this study.

1.7 Hydrological modelling

The water cycle is a complex interacting system, above and below the surface of the Earth (Fig. 1.6). The partitioning of the water into the major reservoirs of ice, fresh water, saline water and atmospheric water is variable in time and depends on a wide range of climatic processes. The water moves from one storage point to another, such as from the ocean to the atmosphere, by a complex system of physical processes of evaporation, condensation, precipitation, infiltration, surface runoff, and subsurface flow (Wikipedia, 2016). Water evaporates from the ocean and land surface; the water vapor is transported by mean of atmospheric circulation and precipitates as liquid (precipitation) or solid precipitation (snow, hail) on the surface. Part of this water is intercepted by trees and vegetation, part provides runoff on land surface, part infiltrates in the soil (subsurface runoff), part recharges groundwater (groundwater runoff), part discharge into streams (channel routing), and part flows out in the oceans to eventually evaporate again (USGS,

2016). During the cycle, water exchange energy and changes different phases: liquid, solid (ice) and vapor. When water evaporates, it acts as an energy sink, seeking energy from its surroundings and cooling the environment. When it condenses, it releases energy and warms the environment. The interacting phenomena can be very different over the water cycle, varying over a wide range of time and spatial scale. In the atmosphere the water residence time is short and largely driven by the regional atmospheric circulation. The terrestrial hydrology strongly interact with the atmosphere, but the spatial time scale is in mostly of the cases concentrated on the basin scale. At the contrary, if we consider the water in the oceans, it can have a the residence time that reach several centuries. If we consider the groundwater processes, physical processes are even considerably slower.

Hydrological modelling tries to simulate this complex interacting system and plays an important role in prediction and mitigation of floods, urban planning, water management, environmental impact and climate impact studies. Depending on the problem that has to be studied, there is a great abundance of hydrological models in literature that can be used. It is very important to choose the model that most accurately describes the processes we are interested in (i.e. soil moisture dynamic, streamflow for operational needs, etc.) and that better conceptualize the problem we are studying. Since the water cycle deals with a huge variety of spatial and temporal scales, the accurate selection of an appropriate model is an important part of the modelling process (Dingman, 2015).

Traditionally, hydrological simulation modeling systems are classified in three main categories: empirical black box, lumped conceptual, distributed physically based systems. The great majority of the modeling systems used in practice today belong to the first and second types. These models require a modest number of parameters to be calibrated for their operation (Refsgaard and Knudsen, [1996]). Despite their simplicity, many models have proven quite successful in representing an already measured hydrograph. A severe drawback of these traditional modeling systems, however, is that their parameters are not directly related to the physical conditions of the catchment. Accordingly, it may be expected that their applicability is limited to areas where discharge has been measured for some years and where no significant changes in catchment conditions have occurred. Although, they are in widespread use, it is now understood that the basic failure of these models to represent catchment response with a small number of parameters is essentially due to their inability to reproduce the dynamic variation of the saturated areas within the catchment (Beven and Wood, 1983). Distributed and physically based catchment models use parameters which are directly related to the physical characteristics of the catchment (topography, soil, vegetation and geology) and operate within a distributed framework to account for the spatial variability of both physical characteristics and meteorological conditions. These models aim at describing the hydrological processes and their interaction as and where they occur in the catchment and therefore offer the possibility of alleviating the shortcomings of the lumped rainfall-runoff models (Beven and Kirkby (1979); Beven et al. (1984); Abbott et al. (1986); Vivoni et al. (2004)). Distributed models permits to simulate distributed properties of the hydrologic processes and the flow discharge along the entire stream network (Refsgaard et al. (1995); Ivanov et al. (2004); Carpenter and Georgakakos (2004); Smith and Eli (1995); Koren et al.

(2004); Yilmaz et al. (2008)). On the other hand, they have also increased the demand of parameterizations and observations required for driving and evaluating the models. Their spatial complexity is perceived to be an obstacle to the proper identification of model components and parameters, increasing the predictive uncertainty of the model (Beven and Freer, 2001).

A correct choice of the parameters for hydrological modelling represent a very important phase of hydrological experiment. Due to the highly non-linear nature of hydrological processes and the fact that parameter describing different physical processes might have the same effect on the discharge, the task is getting more complicated to be accomplished when the amount of parameters is increased. In models with several parameters, changes of some parameters might be compensated by others and and internal interdependency among parameters affects more than one physical process, so that the single effect is difficult to be isolated. In some cases very different set of parameters values may give nearly equivalents fits, while in other cases model output can be insensitive to the value of one or more parameters. Best fit values can change function of the specific characteristic of the basin, or within a different time period inside the same catchment. For all the aforementioned reasons, model parameters that are not known a-priori needs calibration to be determined properly. The input data of the parameter-estimation set are entered in the model and are systematically adjusted to which values gives the "best" fit between modelled and measured outputs. The fit can be judged quantitatively considering comparison between simulated and misurated hydrographs or flow duration curves, scatterplots etc. (Martinec and Rango, 1989). Calibration procedures can be carried manually (trying to understand the sensibility of the model, varying manually the single parameters within a range) or using automated multiobjective optimization routines functions (such as PEST; Doherty and Johnston (2003)). The first approach can be time demanding but permits to go more in deep to understand the influence of the single parameter on the description of the physical processes and the resulting hydrograph. On the other hand the automated process is more efficient but requires a bigger amount of runs and is more computationally costly.

Once that the parameters are selected, the performance testing should be evaluated by graphical and numerical comparison of modeled and measured output for situations not used in the parameter estimation process. This process is known as validation and represent the final part of the evaluation of the model performance. This part permits to verify that the parameters have not been over calibrated on the sigle event used for calibration, and the model can be used with a certain confidence also to produce reliable results in slightly different conditions (different event, different time period, different river section).

Finally, models implemented for extreme events prediction are required to be reliable and portable, computationally fast, and relatively simple schematization. Although empirical models have been successfully employed in this field, nowadays hydrometeorological forecasting problems call for continuous, spatially distributed models, because of their ability in estimating initial conditions (soil moisture distribution) in combination with distributed forcing (rainfall, temperature, radiation) provided by real time measure-

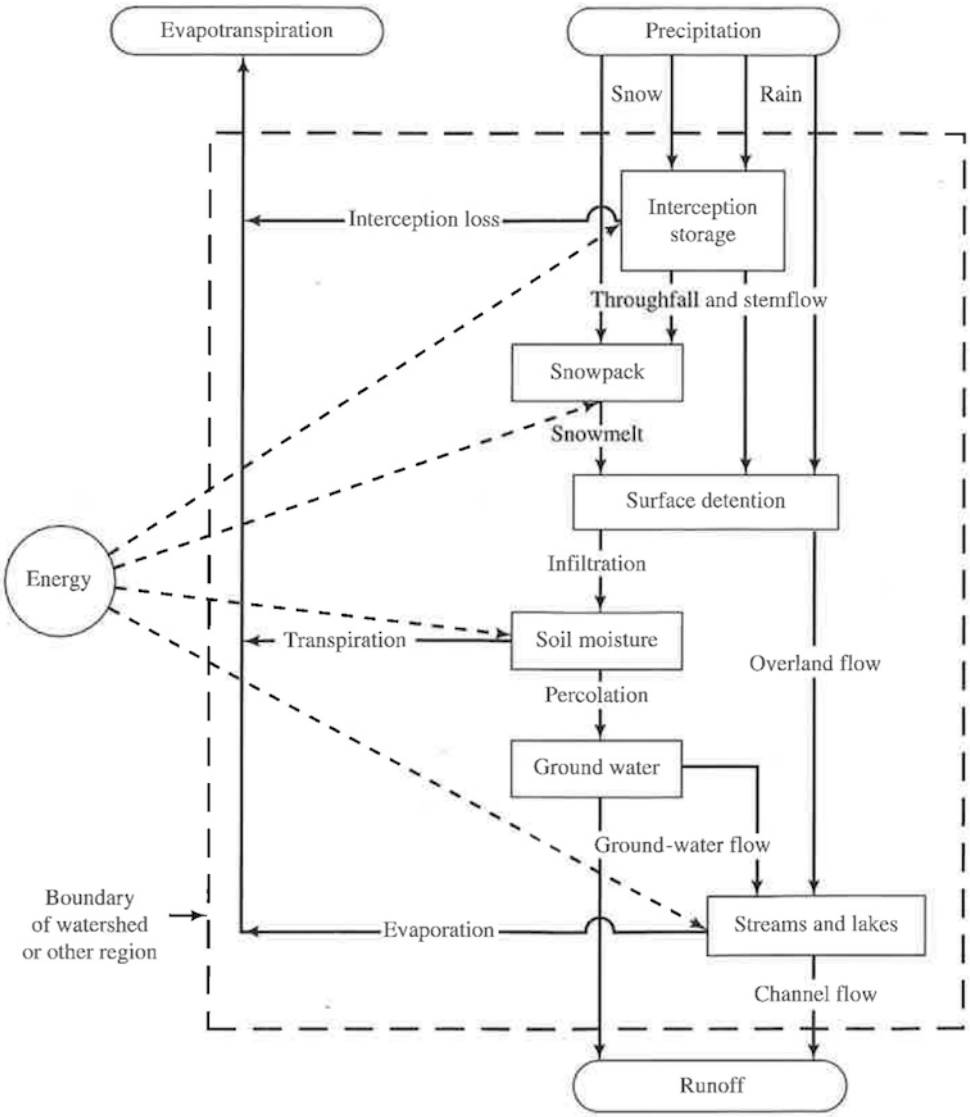

Figure 1.6: Principal storages and pathways of water in the hydrological cycle from Dingman (2015)

ments (meteorological radars, satellites, ground network measurements) and meteorological models (Reed et al., 2007). The WRF-Hydro model is a distributed hydrological state of the art tool developed in to link the terrestrial hydrology to the atmospheric modelling and is the hydrological modelling suite used in the framework of this thesis. A deeper description is given in section 2.4.

1.8 Modelling land-atmosphere interactions: Land Surface Models

Understanding the complex interactions between hydrology, ecology and atmospheric processes represent a key issue to describe the water cycle (Rodriguez-Iturbe (2000); Bates et al. (2008)). Land-surface is located at the borderline between atmosphere and hydrology and needs a cross-interdisciplinary approach to be studied and understood in its complexity.

A land surface model attempts to simulate the partitioning of net radiation at the surface, describing the absorbed radiation at the surface, the emission of thermal and infrared radiation, the latent and sensible heat losses associated to evaporation and transpiration and to energy diffusion on the soil. The first approaches to land surface modelling depicted land surface as an electric system, in which the rate of exchange is regulated by the gradient between one point at the surface and one point in the atmosphere (such a vapor pressure, temperature or carbon dioxide) and controlled by a number of resistances that depends on local climate and internal properties of vegetation and soil (Overgaard et al., 2006). From this first initial schematization (Penman, 1948), the models have been enriched in complexity, including a resistance layer or "big leaf model" to describe evapotranspiration (Monteith (1965); Monteith and Unsworth (2007); Mauser and Schädlich (1998)), the differences between vegetation patch and bare soil and evapotranspiration and transpiration (Avissar and Pielke (1989); Noilhan and Mahfouf (1996); Mengelkamp et al. (1999)). From a single layer model, the land surfece modelling has been further developed to include two layers (Shuttleworth and Wallace (1985); Sellers et al. (1996); Daamen and Simmonds (1996); Daamen (1997)) and to a multi-layer approach with a complex vertical structure (Baldocchi and Harley (1995); Gu et al. (1999)). In addition to that, the exchanges of water and heat at the vegetated land surface has been linked to exchanges of CO2 (Sellers et al. (1996); Gu et al. (1999)).

In general, all the LSM are based on a solution of the energy balance equation and contains sophisticated parameterizations of vegetation and root zone. These kinds of energy-based LSM are one-dimensional column models that describe in great detail the root zone and vegetation interaction and helps to describe the moist and heat fluxes between land surface and atmosphere for different vegetation types and climatic conditions.

Energy based LSMs are used in atmospheric modelling to provide informations on all the fluxes and state variables required at the land-atmosphere boundary. Land surface and atmosphere exchange energy and water fluxes and control the movement between surface and the underground, between the surface and the atmospheric boundary layer and between the planetary boundary layer and the atmosphere. Fluxes of heat and water

from the land surface to the atmosphere affect humidity, temperature and air pressure in the atmosphere. This feedback is highly varying from the meteorological scale we are considering, but it has been proved in several studies, especially on PBL dynamics and the interaction between vegetation (Brubaker and Entekhabi (1996); Kim and Entekhabi (1998)) and soil types and local mesoscale circulations (Segal et al. (1988); Pinty et al. (1989); Cuenca et al. (1996)) . Temporal and spatial distribution of precipitation is also sensitive to the choice of the land-surface scheme (van den Hurk et al. (2002); Zeng et al. (2002)). Land surface models have been implemented in most of the atmospheric models. Even most of these describes the vegetation layer and the root zone exchanges in great detail, they consider only partially the interactions between root zone and the canopy, surface routing and lateral surface and subsurface flows between cells are rarely considered or strongly approximated (Overgaard et al., 2006). This aspect may lead to inaccurate model predictions in areas where groundwater and surface water are closely connected (York et al. (2002); Chen and Hu (2004)). At the contrary, most of the distributed hydrological models describes the runoff partitioning in surface, subsurface and groundwater flow in great detail but treat the meteorological forcing in a semplicistic way, or strongly conditioned by the atmospheric model coarser resolution. The lack of feedback between changes in land-surface or hydrological properties to the atmosphere can potentially lead to errors in simulations in areas in where this contribution is important. A dynamic coupling between atmospheric models and hydrological models by mean of LSM can feel the gap in describing land-atmosphere interactions. Coupled modelling system could provide informations on how the atmosphere will respond to changes in the hydrological and land-surface properties at the hydrological scale and providing informations on the consequences of neglecting atmospheric feedback in hydrological scenario simulations.

A growing number of studies has identified that a more integrated representation of land atmosphere and hydrology interactions by means of coupled model system may led to the situations where surface interactions feedback will significantly help to produce more accurate predictions (Chen and Dudhia (2001); Jasper et al. (2002); Overgaard et al. (2006); Maxwell et al. (2007); Anyah et al. (2008); Maxwell and Kollet (2008); Lowrey and Yang (2008); Jung et al. (2010); Koster et al. (2010); Delire et al. (2011); Balsamo et al. (2011); Moreno et al. (2013); Larsen et al. (2014)).

The Multi-Physics (MP) version of the Noah land surface model (Noah-MP) is the LSM used in this PhD study to link the WRF atmospheric model to the WRF-Hydro hydrological suite. A complete description of the Noah MP is given in section 2.3.

Chapter 2

Hydrometeorological modeling: the WRF model and the WRF-Hydro suite

2.1 Introduction

Modelling atmospheric processes and terrestrial hydrology requires high resolution models to properly reproduce the characteristic features of the hydro-meteorological cycle, especially over complex topography areas. In this chapter the modelling tools used in this PhD study, such as WRF (section 2.2) and WRF-Hydro (section 2.4), are described. When the two model suites are coupled, Noah-MP land surface model has been used to pass moisture and heat fluxes from atmosphere to the surface and viceversa (section 2.3). A particular emphasis is given to the importance of an appropriate choice of model settings both for describing atmospheric and hydrological processes (sections 2.2.1 and 2.4.1). Finally, a brief summary on the state of the art research concerning fully coupled studies is given (section 2.5).

2.2 WRF Model

The computational model used for this study is the Advanced Research Weather Research and Forecasting model (ARW-WRF). It is a fully compressible, 3D, Eulerian, nonhydrostatic model conservative for scalar variables. It is a next-generation mesoscale numerical weather prediction system designed to serve both operational forecasting and atmospheric research needs. The developing of WRF model has been a collaborative partnership, principally among the National Center for Atmospheric Research (NCAR), the National Oceanic and Atmospheric Administration (the National Centers for Environmental Prediction (NCEP) and the Forecast Systems Laboratory (FSL), the Air Force Weather Agency (AFWA), the Naval Research Laboratory, the University of Oklahoma, and the Federal Aviation Administration (FAA). WRF allows researchers the ability to

conduct simulations reflecting either real data or idealized configurations. WRF is suitable for a broad spectrum of applications across scales ranging from meters to thousands of kilometers. It uses a terrain following hybrid sigma-pressure vertical coordinate. The grid staggering is the Arakawa E-grid. The same time step is used for all terms. The dynamics conserves a number of first and second order quantities including energy and entropy (Janjic, 1984). The WRF model supports a multiple domain nesting. This kind of technique allows resolution to be focused over a region of interest by introducing an additional grid (or grids) into the simulation. The nested grids are rectangular and are aligned with the parent (coarser) grid within which they are nested. Additionally, the nested grids allow any integer spatial and temporal refinements of the parent grid. The boundary conditions of the finer grid are provided by the interpolation of the coarse grid. The way of interaction between the two grids can be 1-way nesting or 2-way nesting: in the first way there is an only way information exchange from the coarse grid to the fine grid; in the second way the information exchange between the grids is in both directions where the fine grid solution replaces the coarse grid solution for coarse grid points that lie inside the fine grid (coarse-to-fine for the fine-grid lateral boundary computation and fine-to-coarse during the feedback at each coarse-grid time step). As the other LAMs, WRF requires boundary condition from other models. In both of the experiment performed in this thesis, the initial conditions are given by the ERA-Interim reanalysis. A brief description or the reanalysis product is given in section 2.2.2. A general model description is given in the present paragraph, but for a comprehensive description, the reader is referred to Skamarock et al. (2008).

High resolution numerical models were originally designed for simulations in specific convective environments in America and Europe (tad). However, the use of WRF model has been extended in recent years in other parts of the globe. The climate and the topography of the area of study strongly affects the physical environmental processes and, consequently, the different parameterizations do not perform in the same way in different parts of the world. For this reason the appropriate scheme has to be chosen in order to well depict the environmental parameters in some specific regions of the world.

2.2.1 Model parameterizations

WRF offers multiple physics options in order to better describe the features of the atmosphere from the mesoscale down to the microscale. The options typically range from simple and efficient to sophisticated and more computationally costly, and from newly developed schemes to well tried schemes such as those in current operational models. The model physics permits to set different parameterization regarding the microphysics, cumulus parameterizations, surface physics, planetary boundary layer and atmospheric radiation physics. A brief description of the different parameterizations is given hereinafter. For a complete description of all the possible model setting, the reader is referred to Skamarock et al. (2008).

The microphysics schemes range from simplified physics suitable for idealized studies to sophisticated mixed-phase physics suitable for process studies and NWP. Cloud microphysics involves all the aspects related to the property of a cloud at the micro-

scale, including droplet concentrations and sizes, ice-crystal formation, interaction among droplets and rain drop formation. Table 2.1 provides a summary of the most used microphysics schemes in WRF.

Table 2.1: Summary of the main microphysics options in the WRF model.

Microphysics		
Scheme	**Description**	**Reference**
Kessler	Warm rain scheme (with no ice) mainly used for cloud modelling idealized studies	Kessler (1969)
Lin (Purdue)	Six class scheme with water vapor, cloud water, rain, cloud ice, snow, and graupel. More suitable for research studies.	Lin et al. (1983)
WSM3	Single moment scheme. Simple and efficient scheme with three categories: vapor, cloud water/ice, and rain/snow. Ice and snow processes suitable for mesoscale grid resolution.	Hong et al. (2004)
WSM5	Slightly more sophisticated single moment scheme than WSM3. It allows supercooled water and mixed-phase processes.	Hong et al. (2004)
Eta (Ferrier)	Used in operational NCEP models. Simple and efficient scheme that predicts the water/ice mixing ratio explicitly. Diagnostic mixed phase processes.	Rogers et al. (2001)
WSM6	Single moment scheme with Ice, snow and graupel. Suitable for high-resolution simulations. A more extended description is given in section 3.4.1.	Hong and Lim (2006)
Goddard	Six-class scheme with graupel, ice and snow. Suitable for high resolution simulations.	Tao et al. (1989)
Thompson	New update of the previous Thompson scheme (2007). It has more complex spectral/binned schemes that adopt look-up tables and new snow size distribution assumptions. Double moment scheme suitable for high-resolution simulations. A more detailed description is given in section 3.4.1	Thompson et al. (2008)
Milbrant 2-mom	Seven-class microphysics scheme with separate graupel and hail. Double-moment cloud, rain, ice, snow, graupel and hail.	Milbrandt and Yau (2005)
Morrison 2-mom	Six-class scheme with graupel. Double moment ice, snow, rain and graupel for cloud resolving simulations.	Hong and Pan (1996)
WDM5	Double moment version of WSM5 scheme. Introduced cloud and prognostic CCN for warm processes. Five-class microphysics with ice.	Lim and Hong (2010)
WDM6	Double moment version of WSM6 scheme. Introduced cloud and prognostic CCN for warm processes. Six-class microphysics with graupel.	Lim and Hong (2010)

The convection parameterization contains different closure assumptions to help the computation of the cumulus scale convection (Prater and Evans, 2002). It describes the phenomena taking place in atmospheric variables such as moisture and temperature of the air column with the start of convection and interaction between the process of convection

and grid-scale dynamics, extracting grid-scale information from the numerical model (Kerkhoven et al., 2006). Cumulus parameterizations are theoretically only valid for coarser grid sizes, (e.g., greater than 10 km), where they are necessary to properly release latent heat on a realistic time scale in the convective columns. While the assumptions about the convective eddies being entirely sub-grid-scale break down for finer grid sizes, sometimes these schemes have been found to be helpful in triggering convection in 5-10 km grid applications. Generally, they should not be used when the model can resolve the convective eddies itself (e.g., 5 km grid). A short summary of the main cumulus parameterization schemes is provided in Table 2.2.

Table 2.2: Summary of the main cumulus parameterization schemes options in the WRF model.

Cumulus parameterizations		
Scheme	**Description**	**Reference**
Kain-Fritsch	Include shallow and deep convection sub-grid scheme.Include downdrafts, updrafts, entrainment and detrainment and CAPE removal time scale closure. A more detailed description is given in section 3.4.1	Kain and Fritsch (1990)
Betts-Miller-Janjic	Operational scheme for the Eta model. It includes deep and shallow profiles. It does not calculate explicitly downdrafts, updrafts and cloud detrainment processes. Column moist adjustment scheme and not fixed relaxation time.	Betts (1986); Janjic (1994)
Grell-Devenyi (GD)	Operational scheme in NOAA/ESRL model. Multi parameter scheme and multiple-closure scheme. Ensemble method with typically 144 sub-grid members. Explicit calculation of downdrafts and updrafts. Includes cloud and ice detrainment.	Grell and Dévényi (2002)
Simplified Arakawa Schubert (SAS)	Operational scheme in HWRF model. Simple mass?flux scheme that includes cloud and ice detrainment. Quasi?equilibrium closure with shallow mixing scheme and momentum transport (only in WRF NMM)	Han and Pan (2011)
Grell-3d (G3)	Improved version of the GD scheme. The spreading of subsidence to neighboring columns makes it suitable both for coarse and high-resolution simulations.	Grell (1993); Grell and Dévényi (2002)
Tiedtke (TDK)	Mass-flux type scheme with CAPE removal time scale, shallow convection, cloud and ice detrainment and momentum transport are included.	Tiedtke (1989); Zhang et al. (2011)
Zhang-McFarlane (ZM)	CESM climate model scheme. Mass-flux CAPE-removal scheme that includes cloud and ice detrainment, momentum transport with pressure term.	Zhang and McFarlane (1995)
New SAS (NSAS)	Updated scheme form SAS with new mass-flux scheme with deep and shallow components and momentum transport with pressure gradient term.	Han and Pan (2011)

The planetary boundary layer (PBL) is responsible for vertical sub-grid-scale fluxes due to eddy transports in the whole atmospheric column, not just the boundary layer.

The PBL schemes determine the flux profiles within the well-mixed boundary layer and the stable layer, and thus provide atmospheric tendencies of temperature, moisture (including clouds), and horizontal momentum in the entire atmospheric column. Table 2.3 summarize the main PBL scheme available for the WRF model.

Table 2.3: Summary of the main PBL schemes in the WRF model.

Cumulus parameterizations		
Scheme	**Description**	**Reference**
Yonsei University	Parabolic non-local-K mixing in dry convective boundary layer. Explicit entrainment layer and PBL depth determined by thermal profile.	Hong et al. (2006)
Mellor-Yamada-Janjic	Operational scheme of Eta model.Turbulent kinetic prognostic energy scheme over the vertical with local vertical mixing.	Janjic (1994)
MRF	Older version of Yonsei University scheme. Non?local?K mixing in dry convective boundary layer and PBL depth and vertical diffusion in atmosphere is determined by critical bulk Richardson number.	Hong and Pan (1996)
NCEP Global Forecast System (GFS)	Operational scheme of GFS. Similar to the MRF scheme, but with Non-local-K vertical mixing in boundary layer and free atmosphere.	Hong and Pan (1996)

The atmospheric radiation processes includes longwave and shortwave schemes with multiple spectral bands and a simple shortwave scheme suitable for climate and weather applications. Cloud effects and surface fluxes are considered. Some of the available radiation schemes are summarized in Table 2.4.

Table 2.4: Summary of the main radiation schemes (longwave and shortwave) in the WRF model.

Longwave Radiation		
Scheme	**Description**	**Reference**
Rapid Radiative Transfer Model (RRTM)	Cloud-interacting spectral scheme with K-distributions. Look-up tables fit is used to more accurate calculations. Multiple bands, trace gases, and microphysics species are accounted. Ozone and CO2 are prescribed from climatology.	Mlawer et al. (1997)
GFDL	Operational scheme in Eta model. It can be used only with Ferrier microphysics. An old spectral scheme with carbon dioxide, ozone and microphysics effects. Ozone and CO2 are prescribed from climatology.	Fels and Schwarzkopf (1981)

Shortwave Radiation		
Scheme	**Description**	**Reference**
MM5 (Dudhia)	Simple downward calculation allowing efficiently for clouds and clear-sky absorption and scattering.	Dudhia (1989)
MM5 (Goddard shortwave)	Spectral method that allows interactions with clouds and the ozone effects.	Chou and Suarez (1999) Chou et al. (2001)
GFDL shortwave	Operational scheme in Eta model. It can only be used with Ferrier microphysics. This spectral scheme takes into account ozone and cloud effects.	Chou and Suarez (1999) Fels and Schwarzkopf (1981)

The surface physic setting can be multi-layer land surface models ranging from a simple thermal model to full vegetation and soil moisture models, including snow cover and sea ice. A brief description of some of the many available LSM option is given in Table 2.5.

Table 2.5: Summary of the main LSM schemes in the WRF model.

Land Surface Models		
Scheme	**Description**	**Reference**
5-layer thermal diffusion	This is a soil-temperature only scheme, with no effects on water. Predicts ground and soil temperature and provide heat and moist fluxes for PBL.	Dudhia (1996)
Noah LSM	Unified NCEP/NCAR/AFWA scheme. Four-soil-layer scheme for soil temperature and moisture. It accounts for snow dynamic and frozen soil physics. A more detailed description is given in section 2.3.	Tewari et al. (2004)
RUC LSM	Six-soil-layer scheme for soil temperature and moisture. It accounts for multi-layer snow, frozen soil physics and vegetation effects.	Benjamin et al. (2004)
Noah-MP LSM	Scheme based on Noah LSM that uses multiple options for key land atmosphere interaction processes. A detailed description is given in section 2.3.	Niu et al. (2011) Yang et al. (2011)

Since the role of the land surface model is a very important topic in this thesis, a compete section is devoted to describe the Noah and the Noah-MP LSM model used in the experiments (section 2.3)

2.2.2 Model initialization: ERA-Interim reanalysis

ERA-Interim in a global atmospheric reanalysis product of the European Centre for Medium-Range Weather Forecasts (ECMWF). Meteorological reanalysis aims to assimilate historical observational data spanning an extended period, using a single consistent assimilation (or "analysis") scheme throughout. The technique of data assimilation is therefore used to produce an analysis of the initial state, which is a best fit of the numerical model to the available data, taking into account the errors in the model and the data. A reanalysis project involves reprocessing observational data spanning an extended historical period using a consistent modern analysis system, to produce a dataset that can be used for meteorological and climatological studies. In addition to that, the reanalyses also use archived data that was not available to the original analyses in the operational mode. The ERA-Interim project was initiated in 2006 to provide a bridge between ECMWF's previous reanalysis, ERA-40 (1957-2002), and the next-generation extended reanalysis envisaged at ECMWF. Originally, ERA-Interim ran from 1989, but then a 10 year extension for 1979-1988 was produced in 2011. It is continuing to run in real time, with database archive updating on a monthly basis. The main objectives of the project were to improve on certain key aspects of ERA-40, such as the representation of the hydrological cycle, the quality of the stratospheric circulation, and the handling of biases and changes in the observing system. These objectives have been largely achieved as a result of a combination of factors, including many model improvements, the use of 4-dimensional variational analysis, a revised humidity analysis, the use of variational bias

correction for satellite data, and other improvements in data handling. The ERA-Interim atmospheric model and reanalysis system uses the analysis cycle 31r2 of ECMWF's Integrated Forecast System (IFS), which was introduced operationally in September 2006. The reanalysis follow the spatial resolution of 60 levels vertical levels (with top level at 0.1 hPa), T255 spectral resolution as spherical-harmonic representation for the basic dynamical fields and a reduced Gaussian grid with approximately uniform 0.7°spacing for surface and other grid-point fields. Fields from the atmospheric model are archived either at the full T255 spectral resolution or on the corresponding N128 reduced Gaussian grid, depending on their basic representation in the model. Fields from the coupled ocean-wave model are saved on its reduced 1.0°1.0°latitude/longitude grid. ERA-INTERIM reanalysis has been used in this PhD thesis to provide initial and boundary conditions for the high resolution model WRF and WRF/WRF-Hydro. In both of the experiments, the boundary conditions are provided every 6 hours from the re-analysis for all the days of simulation. The initial conditions are given at the 00 UTC of the initialization day.

2.3 NOAH and Noah MP LSM

The Noah LSM is a third generation 1-dimensional land-surface community model, developed in 1993 from a scientific collaboration among public and private institutions, such as Office of Hydrological Development (OHD) of the National Weather Service, National Environmental Satellite Data and Information Service (NESDIS), NASA, NCAR, the U.S. Air Force, and Oregon State University and other universities. (Ek et al., 2003). The objective of these studies was to develop a state of the art LSM suitable for use in National Center Environmental Prediction (NCEP) operational weather and climate prediction models. In this effort, several intercomparison projects have been carried on, as described in the paper of Chen (2005). The Noah LSM architecture was initially implemented from the Oregon State University (OSU) model (Mahrt and Pan (1984) and Pan and Mahrt (1987)), originally developed in mid 80's. The OSU model used a two layer soil model to calculate soil temperature and soil moisture and a simple plant canopy conductance schematization (Mahrt and Pan, 1984). From this first early development, the current version of Noah (3.0) has been enriched of a four layer soil representation, an improved canopy conductance formulation (Chen et al., 1996), surface runoff and infiltration (Schaake et al., 1996), schemes for bare soil evaporation and vegetation phenology (Betts et al., 1997), thermal roughness length (Chen et al., 1997a), green vegetation fraction schemes (Gutman and Ignatov, 1998), snow cover and sea ice schematizations (Ramsay, 1998), frozen soil and snowpack physics schemes (Koren et al., 1999), snow-surface energy budget calculations (Ek et al., 2003) and seasonal variability of the surface emissivity (Tewari et al., 2004). The time development of the model improvements is summarized in Gochis et al. (2013) and extensively described in Chen (2005) and Ek et al. (2003).

The Noah LSM has been widely tested and successfully validated for several off-line and coupled simulations at a wide range of spatial and temporal scales (Berbery et al. (1996, 1999); Berbery (2001); Berbery et al. (2003)Chen et al. (1996, 1997a); Berbery

(2001);Chen et al. (1997b); Betts et al. (1997); Qu et al. (1998); Wood et al. (1998); Yucel et al. (1998), Chen and Mitchell (1999); Hinkelman et al. (1999); Koren et al. (1999); Schlosser et al. (2000); Angevine and Mitchell (2001); Chen and Dudhia (2001); Slater et al. (2001); Bowling et al. (2003); Marshall et al. (2003); Mitchell et al. (2004); Boone et al. (2004); Chen et al. (2007)). It is currently used coupled to the WRF model, as one of the available LSM options (Skamarock et al., 2008).

The Noah LSM model numerically integrates the governing equations of the physical processes of the soil-vegetation-snowpack medium, calculating several surface variables such as soil moisture, soil temperature, skin temperature, snowpack depth, snowpack water equivalent, canopy water content, water and energy fluxes (Mitchell (2001); Ek et al. (2003)).

Noah LSM has been widely validated in several intercomparison projects such as the Project for Intercomparison of Land surface Paramerizations (PILPS) (Henderson-Sellers et al., 1995), the Global Soil Wetness Project (Dirmeyer et al., 1999), and the Distributed Model Intercomparison Project (Smith et al., 2004) (Gochis et al., 2013).

Nevertheless, some aspects of the model structure has been highlighted to be improved (Niu et al., 2011). Noah LSM does not explicitly calculate photosynthetically active radiation (PAR), temperature, energy, water, and carbon fluxes of the canopy. In addition to that, for thick snow layers it tends to underestimate the ground heat flux, becoming more prone to snowmelt. Noah's soil column extend to maximum 2 m depth and is not able to capture the critical zone under 5 m to which the surface energy budgets are most sensitive (Maxwell and Kollet (2008) and Niu et al. (2011)). The Noah frozen soil routine dynamic is too reactive some vegetation and climate conditions, resulting in less infiltration of water originated from snowmelt processes and in too much surface runoff in spring or early summer. Finally, the system has too short memory of the antecedent weather or climate conditions because of the adoption of a free drainage scheme (Niu et al., 2011).

In addition to that, the ongoing research and novel inter-comparison projects has pushed towards the exigency of a multi-phisic description of LSM (Entin (1999); Guo et al. (2006); Dirmeyer et al. (2006)). A multiple description of LSM offer the potential to mimic a multi-model behavior and are well suited for ensemble models analysis. In this framework, the Noah-MP model has been developed from the original Noah LSM. Noah-MP use multiparametezations options for key land-atmosphere processes in order to facilitate ensemble climate predictions, to identificate the most critical physical processes controlling land-atmosphere coupling and to identify optimal combinations of parameters and model differences (Niu et al., 2011). Noah-MP contains a number of improvements including a separate vegetation canopy layer that computes ground temperature and canopy temperature separately (Yang and Friedl (2003) and Niu and Yang (2004)). It defined the canopy using a canopy top and bottom, crown radius, and leaves with prescribed properties. The gaps of the canopy are considered to compute absorbed solar radiation considering sunlight fraction and shaded leaves (Dickinson (1983); Niu and Yang (2004)) and a Ball-Berry stomatal resistance scheme (Ball et al. (1987); Collatz et al. (1991, 1992); Sellers et al. (1996); Bonan (1996)) is used to relate stomatal

resistance to leaf photosynthesis. In addition to that, Noah-MP contains several improvements in terms of surface hydrology (Niu et al., 2011): it considers a physically based three-layers snow model (Yang et al., 2011), with liquid water storage and melt/refreeze capability, a snow-interception dynamic and sublimation in the canopy-intercepted snow (Yang and Niu (2003) and Niu and Yang (2004)). Noah MP also implement a simple groundwater model with a TOPMODEL based runoff scheme (Niu et al., 2005, 2007), and multiple available options surface water infiltration and runoff. Finally, a short term dynamic vegetation model (Dickinson et al., 1998) and an improved frozen soil scheme has been introduced (Niu and Yang, 2006). The multi-physic parameterization has been proved to add several contributions in reproducing snow dynamics with a more permeable frozen soil and a more accurate simulation of the snow melting processes. Noah-MP also improves the reproduction of surface fluxes, skin temperature in dry seasons and timing of the runoff peaks (Niu et al., 2011).

2.4 WRF-Hydro Model

The WRF-Hydro system is a a fully distributed, 3-dimensional, variably-saturated surface and subsurface flow model. It was originally designed as implementation of the Noah land surface model in terms of surface overland flow and subsurface saturated flow, taking into account increased complexity in land surface states and fluxes and providing physically-consistent land surface flux and stream channel discharge information for hydrometeorological applications (Gochis and Chen, 2003). The need of adequately resolve the dominant local landscape gradient features responsible for gravitational redistribution of terrestrial moisture led to the development of a subgrid disaggregation-aggregation procedure to map land surface processes into a to a much more finely resolved terrain routing grid. From the initial efforts of Gochis and Chen (2003), further improvements has been added in terms of terrain routing, hydraulic routing model, reservoir routing model, reach-based hydrologic channel routing models, and baseflow estimation routine. This improved LSM model system gradually became a physics-based, fully coupled land surface hydrology-regional atmospheric modeling designed to facilitate easier coupling between the WRF model and components of terrestrial hydrological models. It can be used both as a stand-alone hydrological modeling architecture as well as a coupling architecture for coupling of hydrological models with atmospheric models (such as WRF, as well as other Earth system modeling frameworks). A detailed description of the WRF-Hydro suite is given by Gochis et al. (2013). Hereinafter a brief summary is given from the WRF-Hydro user manual Gochis et al. (2013), in order to understand the main model features.

When WRF-Hydro is coupled to the WRF regional atmospheric model, the forcing data is provided by the atmospheric model with a time-frequency specified in the WRF model namelist, corresponding to the land surface model time-step. When run in a stand-alone mode, these forcing data are provided as gridded input time series. The required forcing data are fields of incoming shortwave and longwave radiation (W/m^2), specific humidity (kg/kg), air temperature (K), surface pressure (Pa), near surface u- and

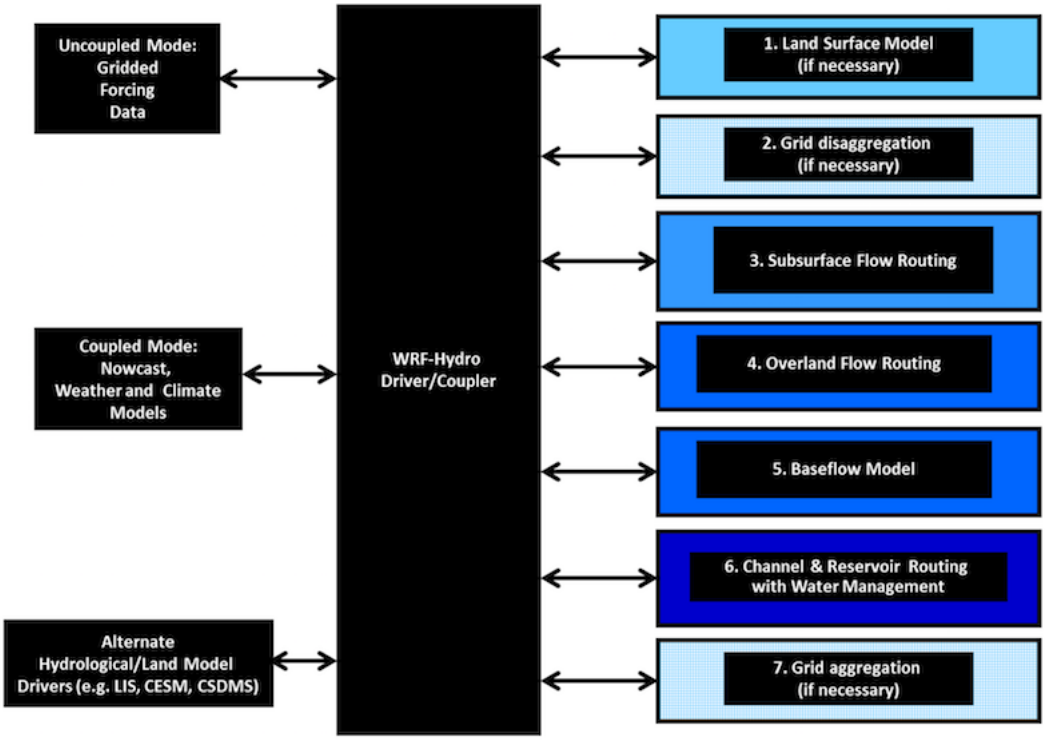

Figure 2.1: WRF-Hydro modelling structure from Gochis et al. (2013)

v-components for wind (m/s) and liquid water precipitation rate (mm/s) from models, observations or reanalysis. In addition to that, Geographic Information System (GIS) tools are used to provide terrestrial informations of stream channel network and water bodies (such as lake, reservoir, and ocean), groundwater basins, flow accumulation and direction. WRF-Hydro model components calculate fluxes of energy and moisture to the atmosphere, water distribution over the surface, flows to stream network and through reservoirs. Model outputs includes surface heat fluxes, surface evaporation components, soil moisture and temperature, surface runoff, stream channel flow, canopy moisture and snow dynamics.

The modelling procedure is illustrated in figure 2.1.

Upon initialization, static land surface physiographic data created using the WRF model pre-processing system (WPS) or other data sources are read into the WRF-Hydro system. In general the most used land cover datasets are provided by USGS 24-type land cover product (Loveland et al., 1995) or by MODIS based land use classification (Friedl et al., 2002). Soil classifications are provided by the 1-km STATSGO database (Miller and White, 1998) for most test studies in the US, but the user can adjust the static data sources, according to their personal needs.

In the first calculation step, the LSM calculates the heat and moisture fluxes. In this part net radiation, sensible and latent heat, interception by the canopy, infiltration

and infiltration-excess, percolation into deep soil layers and ponded water depth are calculated to depict the soil thermal and moisture states. Some of the land surface variables (infiltration excess, ponded water depth and soil moisture) are disaggregated from the coarse LSM grid, to the higher resolution terrain grid, using a time-step weighted method (Gochis and Chen, 2003). The disaggregation loop divides the specific hydrologic state variables from each land surface model pixel into integer portions, according to a specified aggregation/disaggregation factor (AGGFACTR). The disaggregated LSM data are passed to subsurface and overland flow terrain-routing modules to start the hydrological routing processes.

Subsurface flow is calculated prior to all the other terrestrial hydrological processes, since the process takes into account both the exfiltration from the fully saturated grid cells and the infiltration excess calculated from the LSM. Lateral flow of saturated soil moisture is calculated using the method of the Distributed Hydrology Soil Vegetation Model (DHSVM) Wigmosta et al. (1994) and Wigmosta and Lettenmaier (1999). The resulting flow includes the effects of topography, saturated soil depth, and saturated hydraulic conductivity values. The slope of the water table approximates the hydraulic gradients between adjacent grid cells. For each time step, the flux of the water on the grid points is approximated as a steady-state solution (Gochis et al., 2013). The saturated subsurface routing methodology of Wigmosta et al. (1994) consider the soil as a single homogeneous column in which a minimum of four soil layers are used in a 2-meter soil column.

Overland flow is calculated when the water depth on a model grid cell exceeds a specified retention depth, depending on the local terrain conditions. The overland routing is formulated according to the diffusive wave formulation of Julien et al. (1995) (CASC2D), as modified by Ogden and Saghafian (1997). In this formulation backwater effects and flow on adverse slopes is allowed in the diffusive wave equation formulation (Ogden and Saghafian, 1997). According to Julien et al. (1995), the continuity equation for a flood wave over land is combined with the diffusive wave formulation of the momentum equation. The resistance is formulated with Manning's equation and requires to specify a roughness parameter for overland flow.

A simple mass balance calculation is performed to represent overland flow discharging into a stream channel. When the ponded water depth of a channel grid cell exceeds the maximum retention depth, water flows into the channel network. The water depth is calculated in any of the grid cells as a combination of the local infiltration excess, the amount of water flowing onto the grid cell from over land flow, and contribution from groundwater flow that exfiltrates. The exceeding surface head from the retention depth is accumulated as stream channel inflow and is added to the channel routing. A 1-dimensional diffusive wave represent the routing of the river flow in the channel network. The inflow to the channel network and lake and reservoir objects are modelled as a one-way process. Water from channels and lakes can not move back to the surface and subsurface routing.

When the channel network and overland flow intersects a lake object, water flows inside the object. In addition to that, no lake evaporation or subsurface exchange between

the land surface and lakes and reservoirs is represented as fluxes from lakes objects to the atmosphere or the land surface. Reservoirs and lakes are represented with a simple level pool scheme that tracks water elevation changes over time, with contributing input and output discharges in and from the pool.

The contribution of baseflow to the stream network, is represented using a simple, empirically-based bucket model which obtains drainage flow from the spatially-distributed landscape. Baseflow model is activated mainly for long-term seasonal simulations, where baseflow contribution must be taken into account especially for low flow periods. Each groundwater basin is represented as a bucket reservoir with a conceptual water depth and associated maximun volume capacity. The groundwater basins in WRF-Hydro are assumed to match the surface catchments and sub-catchments. The reservoir acts as a simple bucket where the baseflow is estimated empirically, by means of an exponential function that depends on basin recharge. Estimated baseflow discharge is input into the river network from the bucket, together with the contributes of lateral inflow from overland flow and Noah-distributed inflow. The total baseflow spilled from the bucket to the river network is equally distributed among all channel pixels within the catchment.

Since the WRF-Hydro model has been built as a modularized architecture, each of the above mentioned routing modules can be switched on or off, depending on the kind of experiment we are interested in. Once that the model preformed all the desired hydrological routing calculations, land surface states and fluxes are updated and then aggregated from the high resolution terrain routing grid to the land surface model grid. Results obtained from these integrations are saved to the model output files and restart files. In the case the WRF-Hydro is used in coupled configuration, the updated state variables are passed back to the WRF model for the next time step integration.

The performed calculations over the high resolution terrain grid (such as overland routing and channel routing) uses a model time step defined by the user that is set accordingly to the grid resolution. This choice has to satisfy the Courant condition, in order to prevent numerical diffusion of the flood wave. The Courant Number, Cn= $c(\Delta t/\Delta x)$, should be less than 1.0 in order to prevent numerical diffusion.

2.4.1 WRF-Hydro Model parameterizations

As discussed in previous section 2.4, each module of the WRF-Hydro suite, describes a set of hydrological and land-surface process. Land-surface interactions are calculated by the Noah-MP LSM that is currently included in the WRF-Hydro suite. Most of these modules require the setting of some parameters in order to produce results not too far from the observations (to a more detailed discussion of the problem of hydrological model calibration and validation, the reader is referred to section 4.4.3). Input parameters are grouped inside parameter tables and permits to calibrate both LSM Noah-MP processes and hydrological processes. Three of the total parameter tables are for calibrating the LSM (VEGPARM.TBL, SOILPARM.TBL, GENPARM.TBL) and depends on land cover, soil type and some soil texture and moisture coefficients.

LSM decides the surface water partitioning between water that infiltrates (I), surface runoff (R) and contributes to the deep drainage. As specified in the equations 2.1 and 2.2, the infiltration rate in Noah-MP is calculated as the minimum between the current surface water rate (H_{sfc}) and the product of the maximum soil infiltration capacity (I_{max}) with the fractional impermeable area (F_{frz}). The runoff rate (R), at the contrary, is the maximum between zero and the difference between the current surface water rate H_{sfc} and the product of the maximum soil infiltration capacity (I_{max}) with the fractional impermeable area (F_{frz}). H_{sfc} is computed from the surface water budget and is calculated as the differences between the total water input (obtained as the sum of rainfall, dewfall snowmelt and storage water at the surface) and the evaporation rate. F_{frz} is function of the soil ice content of the surface layer, while I_{max} depends on soil texture and soil moisture content of the upper soil layer.

$$I = \min\left(H_{sfc}, F_{frz} I_{max}\right) \tag{2.1}$$

$$R = \max\left(0, H_{sfc} - F_{frz} I_{max}\right) \tag{2.2}$$

Both the infiltration rate and runoff equations (equation 2.2 and equation 2.1) depend on the maximum surface infiltration capacity (I_{max}), function of the four tunable parameters of maximum surface moisture content (SMC_{max}), surface moisture content at the wilting point (SMC_{wlt}), $REFKDT$ and $REFDK$ (Verri et al., tted).

$REFKDT$ represent the infiltration/runoff generation parameter or infiltration factor that influence surface partitioning and the total runoff partitioning in surface and subsurface runoff (Schaake et al. (1996), Givati et al. (2016)). $REFDK$ is the reference soil hydraulic parameter that corresponds to the scaling of saturated hydraulic conductivity for silty clay loam (Givati et al., 2016). Soil moisture content parameters (SMC_{max} and SMC_{wlt}) are function of the soil type. The I_{max} is calculated in equation 2.3, where H_{max} is the maximum surface water level and C_{inf} is the infiltration capacity.

$$I_{max} = H_{max} \frac{C_{inf}}{H_{max} + C_{inf}} \frac{1}{\Delta t} \tag{2.3}$$

C_{inf} is computed by the formula in equation 2.4, function of the most superficial soil layer. $\Delta z(k=1)$ is the thickness of the most superficial soil layer, Δt is the model time step, $SMC(k=1)$ is the soil moisture content at the upper soil layer (Verri et al., tted).

$$\begin{aligned} C_{inf}(k=1) = \Bigg[\sum_{k=1}^{N} \Delta z(k=1)(SMC_{max} - SMC_{wlt}) \cdot \\ \left(1.0 - \frac{SMC(k=1) - SMC_{wlt}}{SMC_{max} - SMC_{wlt}}\right) \Bigg] \cdot \left(1 - e^{\frac{SMC_{max} \cdot REFKDT}{REFDK} \Delta t}\right) \end{aligned} \tag{2.4}$$

Finally, the groundwater drainage term is given by the equation 2.5, function of the deepest soil layer (soil level k=4) (Verri et al., tted).

$$Q_{bot} = SLOPE \cdot DKSAT \cdot \left[\max\left(0.01, \frac{SMC(k=4)}{SMCmax}\right)\right]^{2B+3} \cdot (1 - Ffrz) \qquad (2.5)$$

$DKSAT$ is the saturated soil hydraulic conductivity and B is a non dimensional coefficient function of the soil texture. Both this parameters depends on the soil type. $SLOPE$ parameter is regulating the gravitational free drainage out of the last soil layer, ranging fro 0.1 to 1.0 and function of nine slope classes prescribed according to Zobler (1986).

The other WRF-Hydro specific tables regard more directly the hydrological routing than the LSM processes and include parameters that regulates channel geometry and roughness, bucket model coefficient, surface routing roughness, lake and reservoir location and size, lateral settings such as lateral surface and subsurface saturated conductivity and hydrological and hydraulic parameters.

In overland flow routing, the resulting runoff is calculated when the depth of ponded water in a grid cell exceeds a specified retention depth ($RETDEPRT$), which is a parameter function of soil type. Ponded water below retention depth value do not move and are subject to future infiltration. Moreover, overland flow routing parameters are linked to surface roughness and determine how fast water moves across the domain and along the channel network. When roughness is higher, the surface flow is slower over the surface and there is an higher the chance that water will infiltrate into the soil prior to reach the channel network. Roughness parameter affects both volume and timing of the simulations. These parameters are function of soil type and default values are specified in Ek et al. (2003). Manning roughness coefficient is function of soil type as well and the default values are defined by Vieux and Moreda (2003). In addition to the parameters in the tables, a distributed scaling factor for overland flow roughness ($OVROUGHRTFAC$) and the surface retention depth ($RETDEPRTFAC$) are also tunable in the high resolution terrain routing grid.

Parameterization of channel routing is linked to stream order values. In general, as the stream order increases towards the channel outlet, Manning roughness coefficients decrease and the channel bottom increase in width and shallower side slopes. For each channel grid cell there is an assumed channel reach of trapezoidal geometry, function of Strahler stream order (Strahler, 1952). Channel parameters side slope, bottom width and roughness are parameters that describes channel routing geometry. Channel elements receive lateral inflow from overland flow. No over-bank flow is considered and the vertical dimension of the channel is effectively infinite. Channel geometry parameters and the lack of an over-bank flow representation some limitations in model river stage comparison with the observations.

Lake/reservoir parameters are required for level-pool routing and are represented by weir and orifice coefficients, weir length, orifice area, reservoir area, and maximum reservoir height at full storage.

WRF-Hydro uses an exponential function for estimating the bucket discharge in the groundwater model as a function of a conceptual depth of water in the bucket (equation

2.6).

$$Q_i = C_i e^{a_i z_i} \tag{2.6}$$

For each baseflow basin i specified within the model domain the bucket model coefficient (C), bucket model exponent ($a_i z_i$) and the initial and maximum depth of water in the bucket model (Z_{init} and Z_{max}) are defined. When the bucket model reach the maximum value of Z_{max}, the bucket spills out and contributes to the baseflow. This simple bucket model is a highly abstracted and conceptualized representation of groundwater processes with no real physical basis.

The ZSOIL variable permits to specify manually the depth of the soil layers, even if the total soil column depth and each soil layer thickness are constant over the whole model domain.

Finally, according to Senatore et al. (2015), also the time step can affect the simulation. Even if it's not considered a tunable parameter, the user has to be aware of the fact that if the time step is increased, the contribution of the LSM feedbacks increases in terms of frequency to the coupled model and can significantly affect the simulation. It impacts how frequently infiltration and other fluxes are calculated. If the land model is called frequently, as a consequence the infiltration is calculated more often and more water tends to infiltrates instead than contributing to the channel network. In addition to that, more frequent land model calls usually result in more infiltration, less runoff and lower peak flows (Senatore et al., 2015):

A proper calibration and validation has been carried both for the meteorological model and hydrological routing, in order to perform the fully-coupled applications. A detailed description of hydrological calibration for the WRF-Hydro seasonal simulation is provided in section 4.4.

2.5 Fully coupled experiments using WRF-Hydro. Small summary of the state of the art

As previously introduced in section 1.8, a coupled modelling system that links the complex interactions of atmospheric processes and terrestrial hydrology represent an opportunity to study the possible situations in which the land surface feedbacks on the atmosphere can significantly affect the simulations. A more detailed representation of the physical processes in terms of vegetation dynamics and terrestrial hydrology that consider runoff lateral water redistribution arise the question wether a coupled model approach can improve on some extent the precipitation predictability (Adler et al. (2003); Seneviratne et al. (2006); Fan et al. (2007); Maxwell and Kollet (2008); Lowrey and Yang (2008); Balsamo et al. (2011); Santanello Jr et al. (2013); Koster et al. (2014)). In addition to that, fully-coupled land atmosphere models can reproduce the water cycle system in only one simulation and obtain outputs that goes from atmospheric variables to fluxes, spatial distribution of soil moisture, snowpack and river outlet.

A wide number of studies has been performed regarding fully coupled hydrometeorological modelling systems. The first studies started with Maxwell et al. (2007) which

coupled the Parflow groundwater model (Jones and Woodward, 2001) with the Advanced Regional prediction system ARPS (Xue et al., 2000) and then with the WRF model. These studies found a strong sensitivity of the land surface fluxes to soil moisture dynamics and convective cell locations. Also the Regional atmospheric model System RAMS (Walko et al., 2000) was coupled with a groundwater reservoir, water table dynamics and channel routing (RAMS-Hydro; Miguez-Macho et al. (2007), Anyah et al. (2008)), finding an increased contribution of the ET to the simulations and increased precipitation. Also more recent studies found a positive contribution of the coupling in the modelling of precipitation and atmospheric variables, coupling several atmospheric modelling suites such as COSMO (Baldauf et al., 2011), CAM (Neale et al., 2010), MM5 (Grell et al., 1994), HIRHAM (Christensen et al., 1996) with hydrological models of different complexity such as Parflow, Soil and water assesment tool-SWAT (Arnold and Allen, 1996), PROMET (Mauser and Bach, 2009), MIKE SHE-SWET (Overgaard and Rosbjerg, 2007), 2007), Hydrologic Model System HMS (Yu et al., 2006) (Goodall et al. (2013); Wagner et al. (2013); Zabel and Mauser (2013); Larsen et al. (2014); Butts et al. (2014); Shrestha et al. (2014)).

In this framework of widely developing fully coupled approaches to study the water cycle, the WRF-Hydro has been tested in different regions of the world in coupled and uncoupled way (Fersch et al., 2014). Some operational versions of the system are used by the Israel Hydrological Service and inside the US National Water model architecture for wether alert system.

The study of Yucel et al. (2015), apply the WRF-Hydro model to assess the skills of flood forecasting based on the WRF Model and the EUMETSAT Multi-sensor Precipitation estimates. He used the WRF-Hydro model in uncoupled configuration, over ten rainfall events that occurred in the Black Sea Region. WRF-Hydro calibration was performed using a manual calibration approach over the Bartin sub-basin and extended to the other uncalibrated sourrounding catchments. The study find that the hydrological model was able to skillfully reproduce the observed hydrograph in terms of hydrograph volume and shape, even if the system was very sensitive to precipitation inputs and the single basin response varied from event to event (Yucel et al., 2015). A fully coupled WRF-Hydro application is performed by Arnault et al. (2016) to study the semi-arid environment of the Sissili catchment in West Africa. The study span over the period March 2003-February 2004 and is performed at 10 km and 2 km in the interior domain and 500m for hydrological routing. The study find that WRF-Hydro predicted more infiltration and less runoff at the beginning of the wet season when soils are still dry, even if the contribution of the coupling has small impacts in terms of precipitation, temperature and evapotraspiration. The overall accordance of the simulated hydrograph produced a good accordance with the observations.

Senatore et al. (2015) applied a three year simulation over the Crati river basin in southern Italy, comparing the outputs of the WRF stand alone simulations with the WRF-Hydro fully coupled and with the available observations over the area in terms of precipitation, soil moisture, soil and heat fluxes, surface temperatures, runoff and deep drainage. Atmospheric grid resolution was set to 2.5 km in the internal domain and the

hydrological routing is performed at 250 m, using the Noah LSM. This comparison study between WRF stand alone and WRF-Hydro fully coupled configurations shows higher differences are observed in terms of surface runoff in which the fully-coupled simulation almost doubled the WRF stand alone surface runoff. Soil moisture exhibit differences as well, especially for drier and warmer atmospheric states. The influence on precipitation was actually lower, since the basin is strongly influenced by sea-atmosheric interactions. Nevertheless a positive effect of the WRF-Hydro coupling on precipitation simulation has been proved.

Another study of Givati et al. (2016), performed the comparison between WRF and WRF-Hydro over the Ayalon basin in central Israel in a flood-prediction system oriented application, at 3 km for the finer resolution atmospheric simulation and 100 m for the hydrological routing. The WRF-hydro simulations are compared with the WRF stand alone atmospheric model and the Hydrological Engineering Center-Hydrological Modeling System (HEC-HMS) simulations. The analysis, at the contrary of the previous study of Senatore et al., focuses more on two winter convective storms events and orographically precipitation driven events. This study found that WRF-Hydro fully coupled experiment produced better results compared to the WRF stand alone precipitation estimates. Nevertheless, situations when the WRF atmospheric model detaches significantly from the observations, are not improved significantly by the WRF-Hydro coupling. More improvement can be more evident in continental interior regions or for longer time-scales simulations. They conclude that more research is needed to better understand the mechanism in play for different type of precipitating systems and time scales.

Finally, the WRF-Hydro model suite has recently been introduced in operational applications by the Israel Hydrologic Service (`http://floods.online/home/MeteorologyMap`) and by the National Oceanic Atmospheric Administration (NOAA) National Weather Service in the USA. In this latter case, the WRF-Hydro model suite represent the basis for the development of the new high resolution National Water Model (NWM) of the NOAA-NWS, operative from August 2016. This new platform is fruit of a collaboration of NOAA with NCAR and a partnership with the Consortium of Universities for the Advancement of Hydrologic Sciences, Inc., the National Science Foundation, and Federal Integrated Water Resources Science and Services partners. For further information about the NWM, the reader to the documentation on NOAA website (`http://water.noaa.gov/documents/wrn-national-water-model.pdf`)

In chapter 4 of this thesis we will compare the WRF stand alone with the WRF-Hydro fully coupled application over the Tiber river basin in central Italy, performing model calibration and evaluation at seasonal scale and expecting higher differences between the two model suites during summer season for convective events.

Chapter 3

WRF stand- alone application to the Pakistan flood 2010: sensitivity to parameterizations and initialization time

3.1 Introduction

Quantitative precipitation forecasts (QPF) at fine resolution are an essential ingredient to address the risk estimation of flood-generating precipitation events in complex orography areas. High resolution simulations are needed in order to study the response of catchments during floodings and to improve risk mitigation. These needs become even more prominent in mountain areas, where small distances correspond to high spatial and altitudinal variations. In this chapter I explore the ability of the WRF model, operated at 3.5 km grid spacing, to reproduce the extreme meteorological event that led to the 2010 Pakistan flood and produced heavy monsoonal rain in the Indus basin. In particular, I analyze the sensitivity of the WRF simulations to the use of different convective closures [explicit and Kain-Fritsch (KF)] and microphysical parameterizations [WRF Single-Moment 6-Class Scheme (WSM6) and Thompson] in reproducing such an extreme event. The impact of using different initial conditions, associated with a different initialization day, is also examined. The outputs of the model in terms of daily rainfall are compared with estimates provided by the TRMM satellite (Kummerow et al., 1998) and by raingauge stations. I also investigate the vertical structure of the atmosphere by means of CloudSat observations, comparing them with the WRF simulations using the DS3 (Distributed Simulation and Stimulation System) simulator (Tanelli et al., 2002) included in the NEOS^3 [NASA Earth Observing System Simulation Suite, Tanelli et al. (2012)]. In the analysis presented here and discussed hereafter, the test case of the 2010 Pakistan flood can be considered as an high impact weather event (HIWE) case study where the ability of WRF numerical weather model is seriously challenged. The conclu-

sions indicate that the quality of the large scale initial conditions are a prominent factor affecting the possibility to retrieve a realistic representation of this event, when using a non-hydrostatic regional atmospheric model.

Most of the results here reported have been published in Viterbo, Francesca, et al. "High-Resolution Simulations of the 2010 Pakistan Flood Event: Sensitivity to Parameterizations and Initialization Time." Journal of Hydrometeorology 17.4 (2016): 1147-1167. This chapter represent an extract of the results produced in the article and the reader is constantly referred to Viterbo et al. (2016) for more detailed informations.

3.2 The predictability of Pakistan 2010 event: state of the art studies

In 2010, Pakistan experienced a major flood event that started in late July and was triggered by persistent heavy monsoonal rains. Nearly one-fifth of the entire territory of Pakistan was submerged during the floods (Houze Jr et al., 2011) and the UN Secretary General Ban Ki-Moon, at the 19^{th} August 2010 General Assembly, defined the consequences of this event as a global disaster.

The predictability of this specific event from planetary and large scale synoptic conditions down to the mesoscale storm structures was explored in Rasmussen et al. (2014), analyzing ECMWF (European Centre for Medium-Range Weather Forecasts) ensemble forecasts: the synoptic pattern largely responsible for the conditions that generated the Pakistan flooding event in 2010 could be predicted over a week in advance with significant confidence (as stated also by the study of Webster et al. (2011)). However, the complex topography of the region also played a significant role in the mesoscale development of the event and in determining the detailed rainfall distribution over the area (Rasmussen et al., 2014). Different available forecast and remote observation products reproduced daily rainfall estimate on July 2010 flood, strongly influenced by their resolutions in capturing the magnitude and the features of precipitation.

Even if the predictability of the event from the large scales was demonstrated by Webster et al. (2011), small differences in the local circulation and interaction with the orographic features of the region could produce different results at the mesoscale (Nie et al., 2016). Sub-grid-scale parameterizations and initial conditions can play different roles in determining the predictability of the event at different scales.

In a recent paper, Ushiyama et al. (2014) discussed forecasts of the 2010 Pakistan flood event provided by the WRF (Weather Research and Forecasting) model at 5 km resolution (KF cumulus parameterization and WRF single moment 3-class microphysics) forced by the NCEP-GFS (Global Forecast System by the National Centers for Environmental Prediction). They show that the dynamically downscaled forecasts predicted reliable amounts of rainfall in the Kabul River basin one day ahead of the rainfall onset, and predicted a high probability of heavy rainfall three days ahead. In this work I adopt a finer and cloud permitting grid spacing (3.5 km versus 5 km) in the innermost WRF domain, which is 7 times wider (3807 km x 2643 km vs 1245 km xŮ 1125 km) than the one used by Ushiyama et al. (2014). This allows us to better capture, also at cloud

permitting resolution, the interaction between the mesoscale circulation and the synoptic situation, over the considered complex topography area, whose role has been crucial for the spatio-temporal evolution of this case study. To do that, a finer vertical grid spacing (42 vs 28 vertical levels) is needed to capture more accurately the topographic role on the spatio-temporal evolution of this case study. Two different microphysics schemes (WSM6 and Thompson) instead of only one (WSM3) have been adopted, as well three different convection parameterization approaches (Kain-Fritsch, Betts-Miller Janjic, and explicit) versus one (Kain-Fritsch).

Again, using the WRF model, Ullah and Shouting (2013) showed that a high mid-tropospheric potential vorticity anomaly led to the development of a strong mesoscale convective vortex and to large scale cyclonic circulation over Pakistan during the summer monsoon of 2010. The symmetric instability consequent to the negative moist potential vorticity anomaly significantly enhanced the vertical ascending and precipitation in the convective area (Ullah and Shouting, 2013). In such applications, however, the details of the parameterizations, boundary and initial conditions adopted in the mesoscale model play a crucial role, and the sensitivity of the results to these factors need to be addressed carefully and better understood, especially in the case of such a high impact weather event over an extremely complex topography area. To address these issues, I analyze the role of different convection and microphysics parameterizations, and I investigate the sensitivity to the choice of the initial conditions of WRF simulations performed at cloud-permitting resolution for the most intense days of the 2010 Pakistan flood (July 26^{th} - 31^{st}, 2010).

3.3 Event overview

In early July 2010, a strong ridge of high pressure began to develop near the Ural Mountains in Russia, creating an "Omega" shaped blocking pattern over Europe throughout all western Russia that lasted for at least two months. This high pressure center created an abnormally active jet stream riding around the perimeter of the blocking into western Pakistan, acting as a carrier of hot and moist air and creating a "supercharged monsoon" associated with unstable atmospheric conditions (Hong et al., 2011). The interaction between strong tropical monsoon surges and extratropical disturbances downstream of the blocking became crucial in triggering the flood (Hong et al., 2011). In normal monsoonal events, the low-level moisture flow originates predominantly from the Bay of Bengal, with smaller contributions from the Arabian Sea (Houze Jr et al., 2011). In this case, however, the low-level anomaly in the moisture flux introduced by the indirect contribution of a La Niña phase in south and southeast Asia, had a strong effect in weakening the eastward moisture transport and in helping to enhance the moisture transport and convergence in the northern Arabian Sea and Pakistan (Hong et al., 2011). In figure 3.1, and figure 3.2 panels a5, b5 and c5 show large scale fields of geopotential, temperature and specific humidity of the ERA-Interim reanalysis (Dee et al., 2011a) at 500 hPa, in comparison with the results obtained in the WRF runs (discussed more deeply in section 5).

This situation represented by the reanalysis resulted in an unusual displacement of the heavy monsoonal stratiform precipitation patterns, which are typical for the wetlands in northeastern India and Bangladesh, towards the arid mountainous region of northern Pakistan. This anomalous flow extended also to lower levels, carrying moisture towards the Himalayan barrier and leading to a favourable environment for the mesoscale rain systems (Hong et al., 2011). The European blocking acted on the persistence of this event. Moist air was blocked inside a mountain region of usually dry air, leading to the anticipation of saturation conditions. This caused a less convective vertical growing of the cells and a more stratiform horizontal extension due to upslope flow, respect to what happens in normal monsoonal events in that mountain region (Houze Jr et al., 2011).

The most consistent heavy rainfall event occurred in late July, from 27^{th} to 30^{th}. Galarneau Jr et al. (2012) gives a good description of the developing of convection, analyzing Meteosat-7 and TRMM images. From late July 27^{th} to 06 UTC of July 28^{th} an intense convective event with evidence of possible widespread stratiform precipitation started to interest southwest Pakistan (Houze Jr et al., 2011; Galarneau Jr et al., 2012). Then the rainfall moved towards the high-mountain region in northern Pakistan and persised over the same region for nearly 24 hours from 12 UTC of July 28^{th} to 12 UTC of July 29^{th}, with a continuous redeveloping of convection. The extremely moist environment increased precipitation efficiency and mitigated the cold pool development that could propagate the convection away from mountains. Finally, on July 30^{th}, only light rain persisted over northern Pakistan area and the highest precipitation shifted over west-central India (Galarneau Jr et al., 2012).

In conclusion, the event was characterized by a close interaction between larger and smaller scales and by a strong orographic component (Rasmussen et al., 2014).

3.4 Experimental set up

The runs analyzed in this study are performed using two domains (Fig. 3.3): an external domain (d01), extending in the range 2.59°N-55.52°N and 50.69°W-96.11°W, resolved at 14 km, and an internal domain (d02), extending in the range 10.12°N-49.84°N and 57.08°W-90.02°W, resolved at 3.5 km grid spacing.

The grid spacing adopted for the innermost domain belongs to the so-called cloud-permitting range and represents a good compromise between computational performances and capability of representing the key details of the complex topography of the HKKH range. This choice is improving what has been done in literature till now: to provide some examples of the state of the art, Ushiyama et al. (2014), Ahasan and Khan (2013), Ullah and Shouting (2013) indeed adopted similar small domain grid spacing (respectively 5 km, 3km and 3 km) but on definetely smaller domains (Kabul river basin and a smaller windows in north-west Pakistan), for the same event. Also Maussion et al. (2011) performed simulations in the area at 2 km, but in the Tibetan Plateau (with less steep local orography) and again over a less extended domain.

Fig. 3.3 shows the two nested computational domains and the orography of the region, obtained from the ETOPO1 dataset (Amante and Eakins, 2009). A two-way

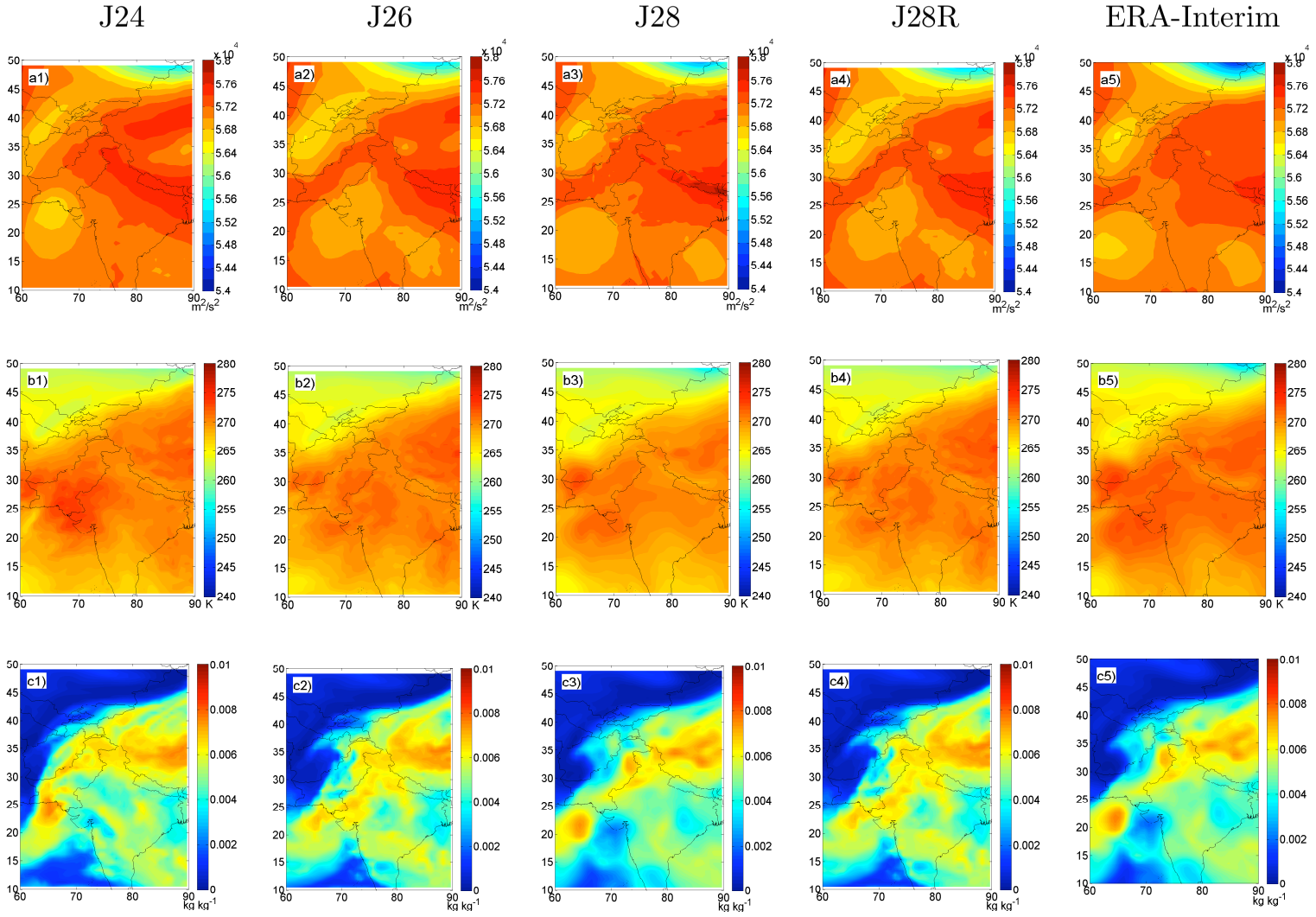

Figure 3.1: Large scale circulation of geopotential (a panels), temperature (b panels) and specific humidity (c panels) at 500 hPa on July 28th at 00 UTC as simulated by WRF J24 (a1, b1, c1), J26 (a2, b2, c2), J28 (a3, b3, c3), J28R (a4, b4, c4) runs and by ERA-Interim reanalysis (a5, b5, c5).

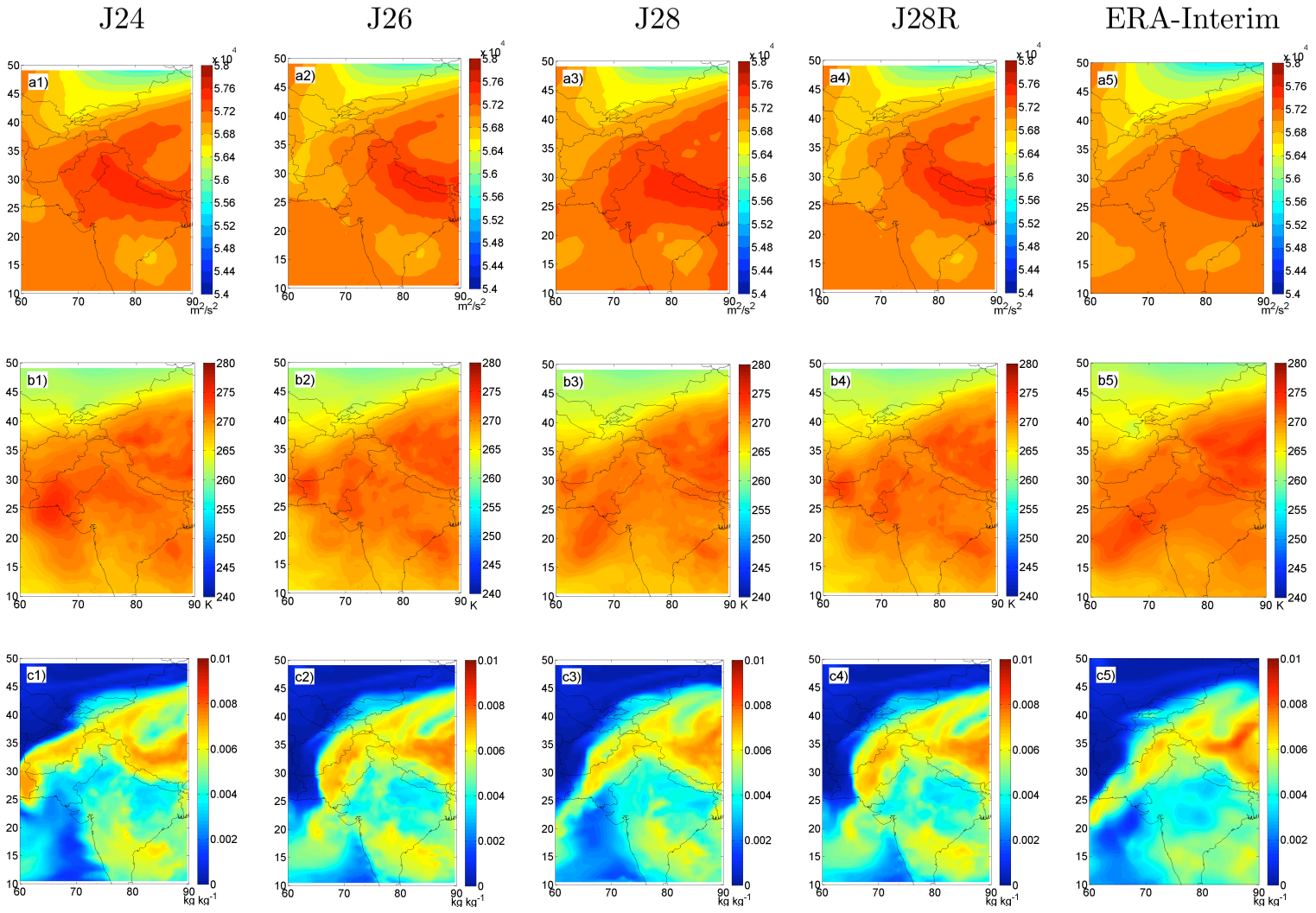

Figure 3.2: Large scale circulation of geopotential (a panels), temperature (b panels) and specific humidity (c panels) at 500 hPa on July 29th at 00 UTC, as simulated by WRF J24 (a1, b1, c1), J26 (a2, b2, c2), J28 (a3, b3, c3), J28R (a4, b4, c4) runs and by ERA-Interim reanalysis (a5, b5, c5).

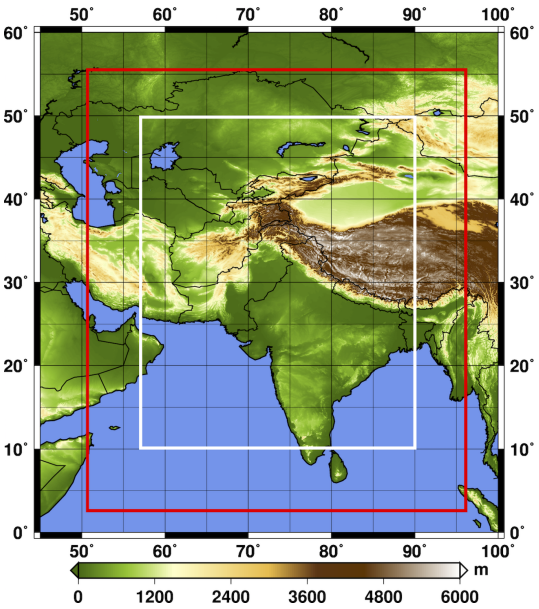

Figure 3.3: The two nested domains used for the simulations: external domain d01 (red box) resolved at 14 km resolution and inner domain d02 (white box) resolved at 3.5 km. The color levels report the orography of the region, provided by the ETOPO1 dataset.

nesting mode is used to couple the two grids. The vertical dimension is discretized with 42 levels. The turbulent parameterization is the Yonsei University scheme (Hong et al., 2006).

The radiation scheme adopted is the rapid radiative transfer model (RRTM) scheme for longwave parameterization (Mlawer et al., 1997), and the Goddard scheme for shortwave parameterization (Chou and Suarez, 1999).

In this experiment, the land use dataset is derived from the United States Geological Survey (USGS) 24-category data at 30 arc-second resolution and the land surface model is the 5-layer thermal diffusion scheme from MM5. The experiment has been carried out in hindcast mode, with boundary and initial conditions provided by ERA-Interim reanalysis fields at the native resolution (0.75°) (Dee et al., 2011b) representing the latest global reanalysis produced by ECMWF. More information about ERA-Interim reanalysis product are given in section 2.2.2.

3.4.1 Microphysical schemes and convective closures

The joint action of the complex topography (due to the presence of the Tibetan plateau and the HKKH range) and of the climatic features of a monsoon-influenced environment make the choice of the convective and microphysics parameterizations difficult (Sardar et al., 2012).

For the convective closure schemes, the choice of a 3.5 km horizontal resolution allows to explicitly resolve (albeit crudely) convective processes (Kain et al., 2006, 2008).

A number of studies investigated numerical simulations in the so-called "grey zone" of spatial resolution, corresponding roughly to 1-5 km, to understand whether convective parameterization is needed at this resolution [e.g. Gerard (2007), Parodi and Tanelli (2010)]. Since no definite conclusion on this issue has been reached [e.g. Yu and Lee (2010)], in this study I opt for running simulations with either a parameterized (Kain and Fritsch, 1990) or explicitly-resolved convection scheme in the d02 domain, while the outermost domain at 14 km adopts always parameterized convection (Kain and Fritsch, 1990)). The choice of Kain-Fritsch as parameterized run is motivated by the results and recommendations of previous studies in the region (Ahasan and Khan (2013), Sardar et al. (2012)).

With regard to microphysics, the leading idea has been to compare the performances of a single-moment scheme, versus a double-moment one when modeling a severe rainfall event, over such an extremely complex topography area with a cloud-permitting grid spacing. For this reason, the single-moment WSM6 (Hong and Lim, 2006) and the double-moment Thompson scheme schemes are selected.

The six-class WSM6 scheme (Hong and Lim, 2006) extends the WSM5 scheme. In this scheme, a new method for representing mixed-phase particle fall speeds for snow and graupel has been introduced. The single fall speed assigned to both classes is weighted by their mixing ratios, and it is applied to both sedimentation and accretion processes (Dudhia et al., 2008).

The Thompson scheme (Thompson et al., 2008) presents a significant number of improvements in the physical processes modeling if compared to earlier single-moment approaches, and it takes advantage of results provided by more complex spectral/binned schemes that adopt look-up tables. The assumed snow size distribution depends on ice water content and temperature and it is represented as a sum of exponential and gamma distributions. Snow assumes a non-spherical shape with a bulk density that varies inversely with the diameter, as found in observations. In the work of Fiori et al. (2014), the authors explored the sensitivity of the Thompson microphysics to the prescribed number of initial cloud droplets N_{tc} created upon autoconversion of water vapor to cloud water. This choice was made to adapt the Thompson microphysics to more maritime rain cases, in the WRF application to a case study of the Genoa flood 2011, in which the main warm rain convective activity was developing from the sea. The results obtained in the Fiori et al. (2014) experiment assess that an higher initial N_{tc} (more maritime values) produces more precipitation. In the Pakistan flood experiment, the warm rainfall occurs on the continental regions of northern Pakistan (more continental than maritime), in a very different environment from the analyses of Fiori et al. (2014). For these reasons we have left the N_{tc} value to its original default value of 100 x 10^6 m^{-3} and this number is not varied in the following analyses.

It is certainly true that using also the single moment WSM6 vs. the double WDM6 microphysics (Lim and Hong, 2010) would have been a worth experiment to perform. However in this study I use WRF version 3.3.1 and WDM6 is a quite new entry in the microphysics parameterization portfolio, still subjected to testing and bug fixes.

In the external domain (d01, 14 km) I use the KF convective scheme and the same

microphysics as in the interior domain.

3.5 Observational data

The orographic complexity of the region under study and the limited availability of meteorological observations in the area represent two of the main challenges in comparing model results with measured data.

The study of Palazzi et al. (2013b) considered and compared different available datasets in the Hindu-Kush Karakoram Himalaya region and evaluated the capability of these observations in reproducing precipitation characteristics and trends. Andermann et al. (2011) produced also a similar study and gave an overview of gridded available precipitation datasets along the Himalaya front. These studies analyzed the differences between the available products, with similarities and discrepancies. Great caution should be used in comparing pixel values of station observations and remote sensing techniques, especially at high temporal resolution (Andermann et al., 2011), particularly when the resolution of observations is coarser than the spatial variability of rainfall. The study of Bytheway and Kummerow (2013) confirms the previous statement, investigating the uncertanties related to the TRMM 3B42 product at 3-h accumulation and 0.25Âř resolution. In their global study of TRMM 3B42 uncertanties over land, they conclude that differences in error characteristics are most prevalent at accumulations below 4mm/h. At accumulations higher than 10 mm/h, the uncertanties of the 3-hour product converge to values between 75% and 85%. They add that high uncertanties values are not surprising for fine temporal resolution data. At the daily scale, uncertainty estimates are grater than 100% for low intensity daily accumulations and decrease to 20% and 40% at higher daily rainfall rates (Bytheway and Kummerow, 2013; Huffman, 1997; Tian and Peters-Lidard, 2010).

In the work of Andermann et al. (2011) the authors stress the difficulties of TRMM-3B42, Global Satellite Mapping of Precipitation (GSMaP) and Climate Prediction CenterâĂŞRainfall Estimates (CPC-RFE) to correctly describe the precipitation distribution at elevations higher than 1 km and to capture precipitation in areas of strong orographic effect. Nevertheless, in the comparison performed by Andermann et al. (2011), the TRMM 3B42 product results to have the smallest bulk error in the monsoon period. Another study by Prakash et al. (2015) has compared the real time TRMM Multisatellite Precipitation Analysis (TMPA)-3B42 and GSMaP estimates against gauge-based measures by the India Meteorological Department (IMD) at the daily scale, using 2000-2010 datasets. They found that these products are able to capture large scale spatial features of monsoon rainfall, but still have region-specific biases. Generally they found a TRMM 3B42 overestimation of 21% and a GSMaP underestimation of 22% over all India, with respect to raingauge based dataset. The largest difficulties in rainfall detection have been found in mountain regions of northeast India (Jammu and Kashmir regions) and in southern peninsular India. Even if their study is referred to Indian area, the Kasmir and are Jummu are neighbouring areas for northern Pakistan, characterized by similar features in terms of monsoon season and high topography.

Taking all this into account, the recommended approach in handling these datasets is a multi-sensor strategy where a collection of information is carefully evaluated, considering the uncertainties of each single dataset (Palazzi et al., 2013b).

Gridded daily rainfall datasets are available from different remote sensing products (e.g. TRMM, GSMaP, etc.). Additionally I have also considered the new PERSIANN CDR dataset (for more information on this dataset the reader is referred to Ashouri et al. (2014)). The precipitation information provided by TRMM, GSMaP and PERSIANN estimates are coherent among each other and provides an encouraging signal on the quality of the satellite estimates available for this specific event.

The vertical structure of the atmosphere has been measured by the TRMM PR 2A25 overpasses and by the CloudSat product, with different times of passing (thus making not easy and immediate their comparison and joint analysis). The TRMM PR 2A25 tracks cut the study area in the south, in a region with only light precipitation; the CloudSat track, at the contrary, passes directly over the main system of interest.

I also have considered raingauge interpolated maps, to provide a source of ground based measurements, instead of only remote sensed estimates, in the daily rainfall comparison.

In this work I rely mainly on remotely-sensed data from TRMM 3B42 and on raingauge interpolated maps as quantitative precipitation estimate (QPE) data sources, while CloudSat data are used for vertical cross-sections.

A quick description of the observational datasets used in this experiment is given in the following paragraphs.

3.5.1 TRMM

The TRMM 3B42 rain products are used as the main QPE source. The purpose of the 3B42 algorithm is to produce TRMM-adjusted merged-infrared (IR) precipitation and root-mean-square (RMS) precipitation-error estimates. The final gridded estimates have a daily temporal resolution and a 0.25°by 0.25°spatial resolution. Spatial coverage extends from 50°S to 50°N. Although the dataset of the TRMM 3B42 product has a 3-hourly temporal resolution, at the finer temporal scales the incidence of sampling errors can be large. For this reason, in our analysis I consider only daily cumulates. A more accurate description of the TRMM mission is given by Kummerow et al. (1998) and by the official NASA product site (`http://disc.sci.gsfc.nasa.gov/TRMM`).

To compare WRF and TRMM daily rainfall fields I have, at first, linearly interpolated WRF fields on a grid finer than the target one (1 km grid spacing), and then I have aggregated the pixels at the TRMM 0.25°resolution (see also Herrera et al. (2015)). I did this transformation in order to conserve the area between the two different grids (the WRF curvilinear and the TRMM linear grid). The fields obtained are focused on a geographic window centered on northern Pakistan (23°N to 40°N in latitude and 66°E to 78°E in longitude). This study area was characterized by heavy precipitation on July 28^{th} and 29^{th}.

The quantitative comparison between WRF and TRMM is computed using statistical scores derived both from the traditional calculation of percentiles (60^{th} and 95^{th}), root

mean square error (RMSE), mean bias (MB), and from the Method for Object-based Diagnostic Evaluation (MODE). This latter method was developed at Research Application Laboratory NCAR/Boulder (USA) and intends to reproduce an human analysiŹs evaluation of the forecast performance. In many cases the traditional scores penalize the performance of forecasts without identifying the cause of the poor performance. An object-based analysis becomes particularly relevant when the model is pushed towards high-resolution and the localization and the episodic characteristics of rain became more important in the verification process. The MODE analysis is performed using a multi-step automated process. A convolution filter and a threshold specified by parameters r and t are applied to the raw field to identify the objects. When the objects are identified, some attributes regarding geometrical features of the objects (such as location, size, aspect ratio and complexity) and precipitation intensity (percentiles, etc.) are measured. These attributes are used to merge objects within the same forecast/observation field, to match forecast and observed objects and to summarize the performance of the forecast by attribute comparison. Finally, the interest value combines in a total interest function all the attributes computed in the object analysis (as shown in Brown et al. (2007), equation 1)), providing an indicator of the overall performance of matching and merging between different observed and simulated objects. In my experiment I have empirically chosen the convolution disk radius and convolution threshold, so that this choice would recognize precipitation areas similar to what a human would identify. After a set of experiments, I fixed the value of the convolution radius to three grid points and the threshold of the convoluted field to 35 mm/day. More information about the MODE technique can be found in Davis et al. (2006a), Davis et al. (2006b) and Brown et al. (2007).

3.5.2 Raingauge stations

Raingauge stations data have been considered as an additional term of comparison for daily rainfall estimates. A set of 98 stations from the Pakistan Meteorological Department (PMD) monitoring network was collected and linearly interpolated over the focus area. Moreover, I have selected 90 stations that fall inside the geographic window of interest, I have compared the gauge measures with the nearest neighbor WRF grid point of the map comparison and I have calculated the associated MB and RMSE. The MB and RMSE calculated comparing with the raingauge dataset are obviously not comparable to the same statistics compared to the TRMM dataset. The raingauge evaluation is computed based on 90 grid points, while the MB and RMSE computed based on TRMM estimates represent a pixel comparison extended to all grid points in the geographic window. Additionally, the two products (raingauges and satellite products) are differently accumulated. The daily rainfall station data are accumulated from 03 UTC for the next 24 hours, so, great caution should be used when comparing them to TRMM data because a 3h offset has to be considered. Finally, the comparison is strongly influenced by the different nature of ground and satellite instruments and by their different weaknesses and strengths in measuring precipitation in areas with complex orography. Nevertheless, in an area of scarce observations, they provide an additional point for the discussion.

3.5.3 CloudSat

The CloudSat satellite mission was designed by NASA to measure the vertical structure of clouds from space and to improve global knowledge of cloud abundance, distribution, structure, and radiative properties. The CloudSat instrument was launched in April 2006, as a part of the A-Train satellite constellation. The Cloud Profiling Radar (CPR) installed on CloudSat is a millimeter-wavelength cloud radar that allows detection of cloud droplets and ice particles forming the cloud masses. The CPR operates at 94 GHz, which represents the best compromise between performance and spacecraft resources, to achieve sufficient cloud detection sensitivity (Tanelli et al., 2008). The data are given to the 2B-GEOPROF product, whose algorithm identifies those levels in the vertical column that contain significant radar echo from hydrometeors and provides an estimate of the radar reflectivity factor for each of these volumes. The CPR provides detailed information on the vertical structure of cloud systems and it represents a relevant source of information for the evaluation of climate and weather prediction models (for more information, see and Stephens et al. (2008)).

To compare model outputs with satellite estimates, it is necessary to have a simulator converting model quantities into equivalent radar reflectivities. The effects of instrumental sensitivity and attenuation by clouds and precipitation have also to be taken into account (Bony et al., 2009; Haynes et al., 2007). For this reason, the NASA Earth Observing System Simulators Suite (NEOS^3) includes the DS3 simulator (Tanelli et al., 2002), that provides forward simulation to evaluate cloud radar and other remote sensing products (Tanelli et al., 2011, 2012). Using this tool, the WRF outputs are compared to CloudSat observations considering the two available satellite tracks over northern Pakistan during the days of the event: granule 22608, recorded on July 28$^{\text{th}}$ around 21:00 UTC, and granule 22615, recorded on July 29$^{\text{th}}$ around 08:00 UTC. The CloudSat observation tracks are provided in Fig. 3.4 and Fig. 3.6 (blue lines). Since the granule 22615 of July 29 $^{\text{th}}$ misses the main observed precipitation core (see Fig. 3.4 panel b6 or Fig. 3.6 panel b7), the results in section 5 are discussed only for granule 22608.

3.6 Sensitivity experiments

3.6.1 Sensitivity to the convective and microphysical schemes

The four different configurations tested in this work are listed in Table 3.1.

Figure 3.4 shows the precipitation fields produced by the WRF model for the different parameterization choices, compared with the TRMM estimates and raingauge observations, in experiments initialized on July 26$^{\text{th}}$ at 00 UTC.

When looking at Exp-WSM6 vs. KF-WSM6 (Fig. 3.4a1 vs. Fig. 3.4a2), we see that the KF scheme produces more precipitation and more organized patterns. This is also true for Exp-Thompson vs. KF-Thompson (Fig. 3.4a3 vs. Fig. 3.4a4). Therefore, in general, it appears that the KF scheme tends to overestimate precipitation and to produce more organized rainfall patterns for my case.

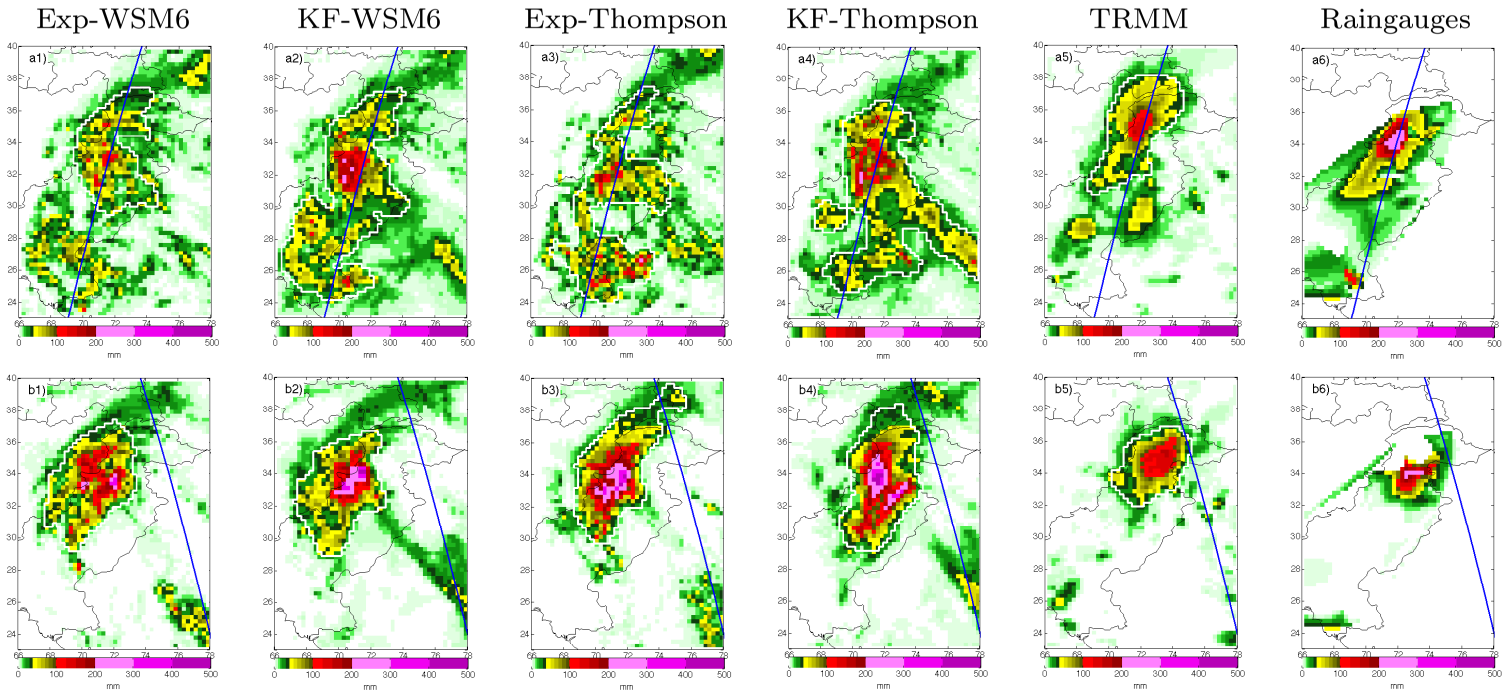

Figure 3.4: WRF Quantitative Precipitation Forecasts and TRMM daily rainfall. From left to right: Exp-WSM6 (a1, b1), KF-WSM6 (a2, b2), Exp-Thompson (a3, b3), KF-Thompson (a4, b4), TRMM (a5, b5) and raingauge observations (a6, b6). All fields have been aggregated at 0.25°resolution in the study area. The top row refers to July 28th 2010 (a) and the bottom row refers to July 29th (b). The blue lines represent CloudSat tracks and the white contour represent the object identified by MODE analysis.

Table 3.1: Experiment configurations.

Configuration	*Convective closure*	*Microphysics*
Exp-WSM6	Explicit	WSM6
KF-WSM6	Kain-Fritsch	WSM6
Exp-Thompson	Explicit	Thompson
KF-Thompson	Kain-Fritsch	Thompson

The statistical evaluation computed for my experiment using traditional statistic and MODE verification analysis is reported in Table 3.2.

The MODE values considered refer to the higher intensity object identified by the verification technique that matches with a corresponding object in TRMM. The white countours in Figure 3.4 represent the MODE objects. The percentile values indicates that all four configurations tested tend to overestimate the rainfall amount compared to the TRMM estimates, especially for 60^{th} percentile on July 28^{th} and 95^{th} percentile on July 29^{th}. The pecentile values confirm the tendency of the KF simulations to overestimate TRMM estimates. On July 28^{th} all the values of the Exp-WSM6 configuration indicate good accordance with TRMM values.

The rainfall intensity given by the percentiles and the localization of the object corresponding to the main precipitation core seem to be best represented by Exp-WSM6. On July 29^{th}, on the contrary, the evaluation doesn't seems univocal: MODE statistical indicators have good agreement with TRMM in terms of total interest and geometric attributes of localization (centroid distance and area ratio) for Thompson microphysic configurations (Exp-Thom and KF-Thom); at the contrary MB and RMSE result the best for Exp-WSM6. All values on July 28^{th} and (especially) on July 29^{th} indicate that the worst results are seemingly obtained using the KF-WSM6 configuration, where the main precipitation core is misplaced and overestimated. As a word of caution, however, we note that the differences in score between the different configurations are not very large, and the highly fragmented appearance of the precipitation fields obtained with explicit convection does not match entirely the TRMM data. In addition to that, with equal convective scheme, the Thompson microphysics presents higher 95^{th} percentile values. If we examine the results of the statistics calculated in comparison with the raingauge datasets (Table 3.3, fourth part), also the MB estimates on July 29^{th} confirm the tendency of the Thompson microphysics to produce higher than observed rainfall amounts (even if closer to measured values than the other simulations). The WSM6 has been found to produce larger values of evaporation rate over the entire atmospheric column in Bryan and Morrison (2012) and in Morrison et al. (2015) with reference to highly-idealized settings with no orography, possibly explaining its reduced precipitation compared to the Thompson scheme. The raingauge statistics produce less underestimation (meaning higher precipitation values) for KF configurations on July 28^{th} and the best RMSE for Ex-WSM6 on July 29^{th}.

Table 3.2: Statistical score analysis for the different configurations for July 28th (upper panel) and for July 29th (lower panel). The first part of the table shows the values of MODE verification analysis of centroid distance, area ratio and and interest. The MODE evaluation refers to the highest intensity object identified in each run that matches with the corresponding TRMM object. The matched objects are shown in Fig.3.4. In the second part the different percentiles (median, 60th, 90th and 95th) are shown . In the third part are reported MB and RMSE. The fourth part of the table shows MB and RMSE calculated between raingauge station measures and associated nearest neighbour WRF grid point. The first three parts of the table use TRMM as reference dataset. The fourth part of the table shows MB and RMSE calculated between raingauge station measures and associated nearest neighbour WRF grid point.

July 28th	$Ex-WSM6$	$KF-WSM6$	$Ex-Thomson$	$KF-Thompson$	$TRMM$
$CENTROID\ DISTANCE$	601	1860	1934	1884	-
$AREA\ RATIO$	0.919	0.452	0.571	0.422	-
$INTEREST$	0.961	0.858	0.851	0.842	-
$PERCENTILE_{60}$	12.19	15.90	12.95	15.15	4.83
$PERCENTILE_{95}$	53.30	67.74	58.99	71.88	52.08
MB	3.73	8.43	5.28	8.03	-
$RMSE$	21.46	26.92	27.31	26.66	-
$MB_{raingauges}$	-20.34	-11.56	-14.60	-10.83	-
$RMSE_{raingauges}$	65.49	65.23	68.81	59.14	-

July 29th	$Ex-WSM6$	$KF-WSM6$	$Ex-Thomson$	$KF-Thompson$	$TRMM$
$CENTROID\ DISTANCE$	967	1208	472	551	-
$AREA\ RATIO$	0.567	0.599	0.544	0.529	-
$INTEREST$	0.914	0.899	0.946	0.940	-
$PERCENTILE_{60}$	3.63	6.55	3.62	5.87	1.04
$PERCENTILE_{95}$	69.99	62.38	83.57	94.04	44.70
MB	6.05	7.27	8.79	8.10.62	-
$RMSE$	30.42	38.12	40.94	40.60	-
$MB_{raingauges}$	-10.41	-10.97	0.44	14.94	-
$RMSE_{raingauges}$	62.54	87.48	96.60	93.46	-

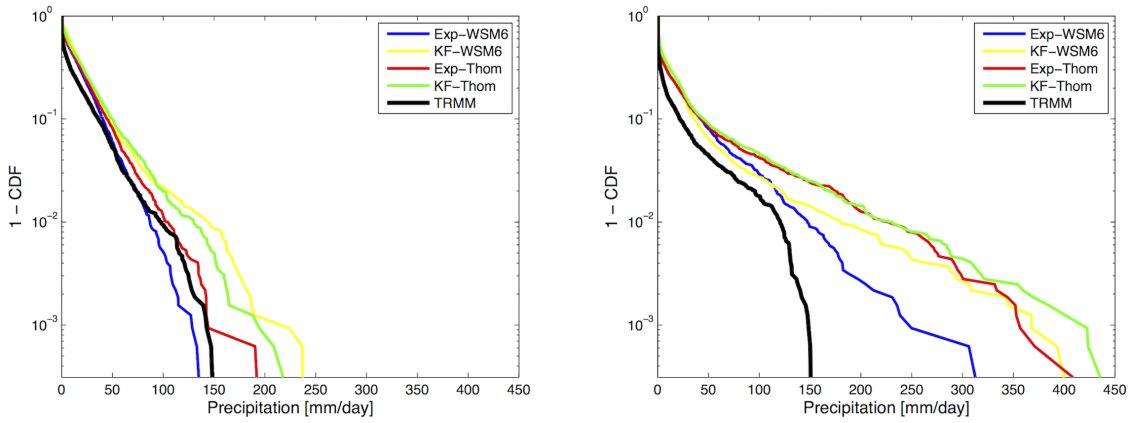

Figure 3.5: Comparison between probabilities of exceedence (1-CDF) for daily rainfall from WRF simulations and TRMM estimates, for July 28th (left panel) and July 29th (right panel). Spatial resolution is 0.25°and the results refer to the whole study area.

The analysis of cumulative distributions permits to understand the variability of the precipitation field and, in particular, the tail of the distribution gives an important information about the probability of exceedace of the highest values of the precipitation field. Figure 3.5 confirms that the Exp-WSM6 simulation produces results which are closer to the statistics of the TRMM estimates. While all the other schemes tend to overestimate the probability of extreme precipitation compared to TRMM, on July 28th the Exp-WSM6 configuration generates distributions which are fairly close to the observations. In this case, the main cause of discrepancy with TRMM (reflected in the statistical scores) is due to a misplacement of the precipitation structures, while intensity and frequency are properly reproduced. On July 29th, all schemes tend to significantly overestimate the observed precipitation.

In Figure 3.4 panels a6 and b6 provides another term of comparison with raingauge ground measurements. Even if, as discussed above, raingauge station present several limitations, the QPE provided by raingauges is higher than TRMM estimates, providing support for the hypothesis of TRMM underestimation instead of a WRF model overestimation. Again, the Exp-WSM6 configuration is the closest to raingauge observations.

3.6.2 Sensitivity to the initialization date

Based on the above results, the configuration with explicit convection and the WSM6 microphysical scheme is selected for further sensitivity analysis. Using this configuration, I perform forecast experiments considering three different initialization days: July 24th (J24), July 26th (J26) and July 28th (J28), all at 00 UTC (Table 3.3). This approach is made in order to choose at first a good model setting to that specific region of the world and then, when the physic of the model is correctly set, the spin up time and the sensitivity to initialization days is investigated. Even if this experiment can be also reversed, this approach is methodologically robust for the above-mentioned reasons, also

Table 3.3: Summary of all the different runs performed in the second part of the experiment.

Run	*Day of initialization*	*Configuration*	*Initial conditions*	*Boundary conditions*	*Hig − res domain*
J26	July 26^{th}	Exp-WSM6	ERA Interim	ERA Interim	10N to 50N 60E to 90E
J24	July 24^{th}	Exp-WSM6	ERA Interim	ERA Interim	10N to 50N 60E to 90E
J28	July 28^{th}	Exp-WSM6	ERA Interim	ERA Interim	10N to 50N 60E to 90E
J28S	July 28^{th}	Exp-WSM6	ERA Interim	ERA Interim	23N to 40N 66E to 78E
J28R	July 28^{th}	Exp-WSM6	WRF J26 restarted at July 28^{th} 00 UTC	ERA Interim	10N to 50N 60E to 90E

considering the state-of-the-art WRF model applications in different parts of the world (e.g Gallus Jr and Bresch (2006), Heikkilä et al. (2011),Fiori et al. (2014), ...).

The different initialization experiments have been chosen considering initialization from 1 to 4 days in advance, every 48 hours. I choose this range, as a good compromise between possible required spin up time of the model and expected model time integration reliability.

The meteorological analysis is performed starting from the large scales (Fig. 3.1 and Fig. 3.2), down to the mesoscale fields for all the different simulations performed, in order to understand the inter-scale interplay of the phenomena. At larger scales, variables such as geopotential, temperature, water vapor mixing ratio are interpolated on the vertical 500 hPa isobar level and compared with the ERA-Interim reanalyses. The synoptic features that led to the severe 2010 events on Pakistan are well reproduced by the model for all its different initializations, if compared with the reanalysis. The geopotential underlines the presence of a strong high pressure block in the northern part of the domain. This blocking high, associated with the presence of smaller scale troughs in the Arabian sea and in the south of Afghanistan, led to the formation of a strong wind blowing from the Arabian sea to the northern part of Pakistan. From the examination of water vapor fields, there is a moisture transport associated to the south-westerly winds that brought a high water vapor quantity up to northern Pakistan. Another source of vapor is given by the moisture flux approaching from the Bay of Bengal. The moisture flux convergence supports the accumulation of moisture during the two days in which the maximum precipitation occurs (July 28^{th} and July 29^{th}). The different model runs exhibit similar large scale circulation, with small differences between the different simulations. Differences start to emerge when we look at the smaller scales, in which the role of orography (valley and ridges) starts to emerge because of the interaction with the small scale circulation. In this case small differences in moisture transport or in wind

circulation reflect deeply the different distribution of the resulting precipitation fields.

Figure 3.6 shows the daily precipitation maps for the crucial days of the event (July 28th and 29th), reporting also TRMM observations and interpolated observations from the available raingauge stations. The J24 run simulates rather well the actual rainfall amounts until July 27th, and then downgrades as the event develops further.

The J26 run offers a good performance even though the simulation is not able to correctly reproduce the patterns of the first days (July 26th and 27th - not shown). For July 29th, the J26 run (Fig. 3.6, panel b2) captures well the main rainfall core, even if it is more widespread and displaced slightly eastward with respect to the observations. The J28 run reproduces well the precipitation pattern on July 28th. On the following day, the J28 run (Fig. 3.6, panel b3) displays a very poor performance, especially when the rainfall pattern of the maximum core is considered. A strong orographic control on the QPF is evident: precipitation is confined to Pakistan plains by the local mountainous range and the most important precipitation core is completely missed. Because of the bad results of J28 for July 29th, I conclude from the map comparison that the J26 run provides a better forecast of the event.

The J28 run produces higher QPF during its first 24 hours of simulation (July 28th), and after that the precipitation rates decreases significantly: a possible explanation for this behavior is the dry-out of the atmospheric column caused by the high precipitation rates on the 28th, together with the lack of time for the moisture from the boundaries to gather in the domain in the following 24 hours. To test this latter possibility I reduce the dimension of the domain: the J28 simulation is run again in the 2-way nesting mode, but this time the original high-resolution domain d02 is downsized to the focus area (23°N to 40°N, 66°E to 78°E) (J28S run). The results obtained for July 29th with the smaller domain do not display any significant improvement, indicating that there must be other causes for the bad performance of the J28 run. In addition to that, the J28S, if compared with J28, shows no sensible dependence of WRF model on small perturbation of initial conditions over the time scale of the experiment.

Figure 3.7 compares the cumulative distributions of daily precipitation for the different initialization dates and for the two target forecast days. The comparison indicates that the J26 run shows a better agreement with the amplitude statistics of the TRMM data. In particular, on the 28th, all other runs (except J24) tend to overestimate the probability of exceedence of precipitation rates larger than about 100 mm/day. On the 29th, on the contrary, the runs started on the other initialization dates lead to an underestimation of precipitation over the area, even if they are still closer to the TRMM estimates.

Statistical evaluation for the different simulations are summarized in Table 3.4.

The statistical scores partially confirm the previous analysis. The J24 simulation displays a good performance on July 28th and the worst performance on July 29th. On the second day the interest value of the MODE analysis is extremely low and the geometrical properties of the forecast-observed objects are highly unrelated. For July 28th, and July 29th J28 appears to have a good statistical evaluation, even if in the map comparison the pattern of the main precipitation core is totally missed. On the contrary of what

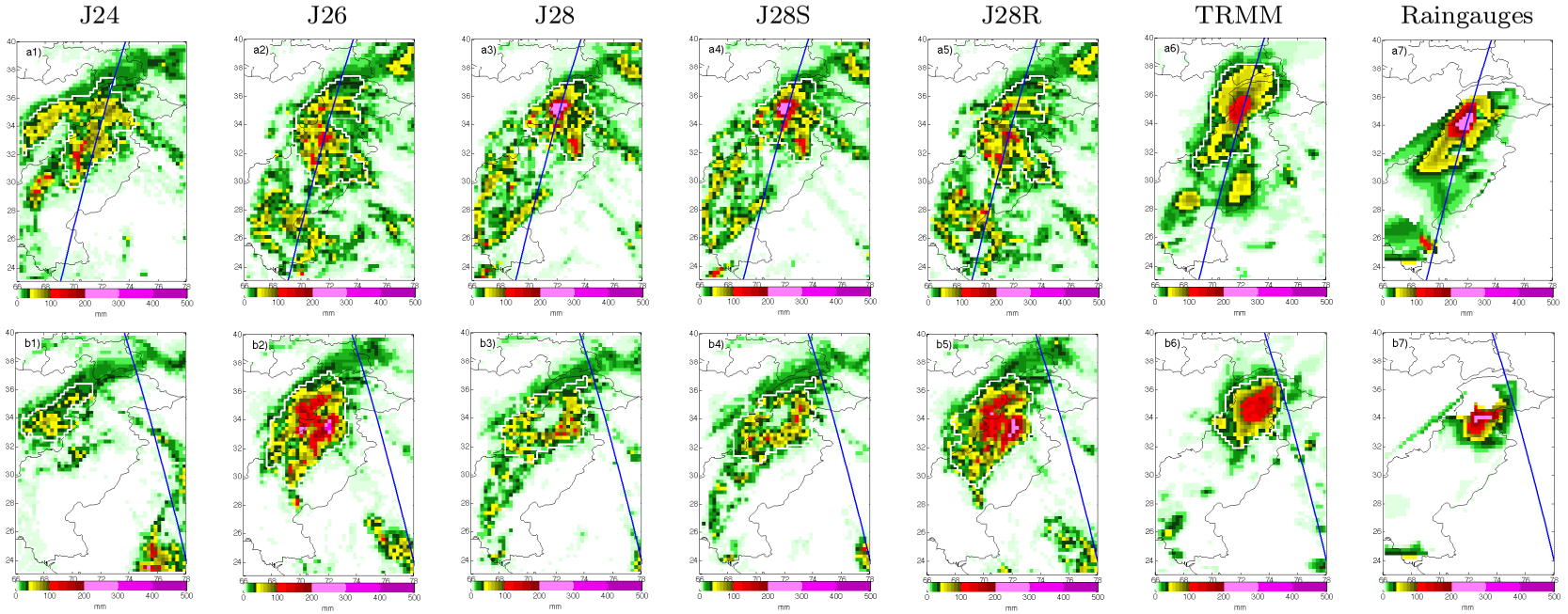

Figure 3.6: First row: 24-hr rainfall cumulates on July 28th given by: J24 (a1), J26 (a2), J28 (a3), J28S (a4), J28R (a5), TRMM (a6) and raingauge stations (a7). Second row: 24-hr rainfall accumulation on July 29th given by: J24 (b1), J26 (b2), J28 (b3), J28S (b4), J28R (b5), TRMM (b6) and raingauge stations (b7). All rainfall fields have been aggregated at 0.25°horizontal resolution. The blue lines represent CloudSat tracks and the white contour represent the object identified by MODE analysis.

Table 3.4: Statistical score analysis for the different initializations, for July 28^{th} (upper panel) and for July 29^{th} (lower panel). The first part of the table shows the values of MODE verification analysis of centroid distance, area ratio and and interest. The MODE evaluation refers to the highest intensity object identified in each run that matches with the corresponding TRMM object. The matched objects are shown in Fig.3.6. In the second part the different percentiles (median, 60^{th}, 90^{th} and 95^{th}) are shown . In the third part are reported MB and RMSE. The fourth part of the table shows MB and RMSE calculated between raingauge station measures and associated nearest neighbour WRF grid point. The first three parts of the table use TRMM as reference dataset. The fourth part of the table shows MB and RMSE calculated between raingauge station measures and associated nearest neighbour WRF grid point.

July 28^{th}	$J24$	$J26$	$J28$	$TRMM$
$CENTROID\ DISTANCE$	568	601	322	-
$AREA\ RATIO$	0.815	0.919	0.750	-
$INTEREST$	0.963	0.961	0.984	-
$PERCENTILE_{60}$	6.53	12.19	6.69	4.83
$PERCENTILE_{95}$	53.29	53.30	55.40	52.08
MB	0.77	3.73	1.96	-
$RMSE$	20.18	21.46	21.80	-
$MB_{raingauges}$	-20.22	-20.34	-9.10	-
$RMSE_{raingauges}$	58.41	65.49	56.31	-

July 29^{th}	$J24$	$J26$	$J28$	$TRMM$
$CENTROID\ DISTANCE$	1544	967	633	-
$AREA\ RATIO$	0.558	0.567	0.924	-
$INTEREST$	0.659	0.914	0.957	-
$PERCENTILE_{60}$	3.28	3.63	2.80	1.04
$PERCENTILE_{95}$	36.25	69.99	39.01	44.70
MB	0.31	6.05	0.28	-
$RMSE$	26.35	30.42	19.24	-
$MB_{raingauges}$	-30.41	-10.41	-18.24	-
$RMSE_{raingauges}$	65.04	62.54	49.83	-

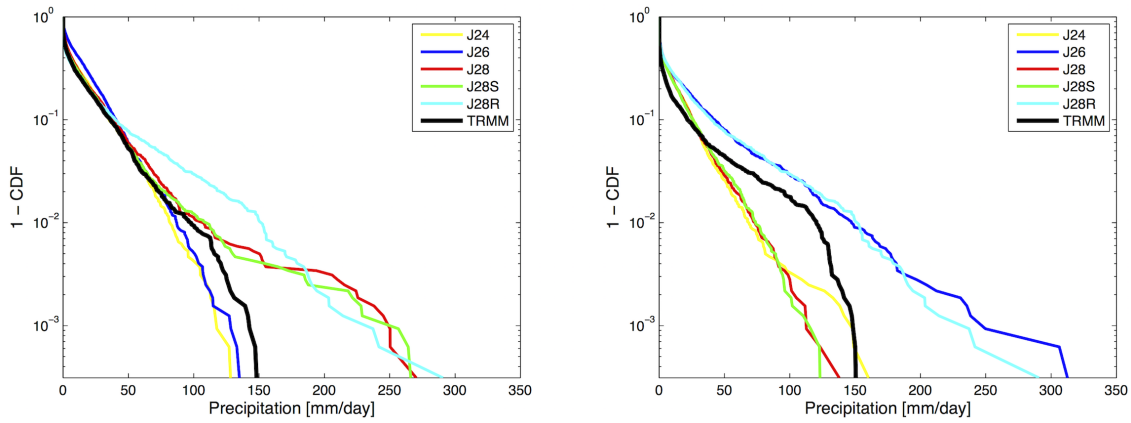

Figure 3.7: Comparison between probabilities of exceedence (1-CDF) obtained from WRF using different initialization days and those derived from TRMM estimates. Left panel: July 28th; right panel: July 29th. The spatial resolution is 0.25°and the results refer to the whole study area.

observed in the map comparison, on July 29th the J28 run result in best values of interest and good percentile values. On the other hand, on July 29th, the 95th percentile confirms the J28 underestimation even if it is still the closest to TRMM values. If we consider that TRMM tend to underestimate in that area (as stated in the previous sections) and the information of the raingauges, we are more prone to penalize an underestimation of the model rainfall values. The TRMM tendency to underestimate, with respect to raingauges is evident from the comparison between MB related to TRMM and the one based on raingauges measures. Even if great caution should be given in the comparison, raingauge MBs are negative (meaning an undestimation of the model, with respect to the raingauges), while the MB of TRMM seems to indicate a general overestimation of the model respect to the satellite estimates. Barring that, the raingauge statistics are rather in accordance with what observed in the previous analysis. The MB and RMSE have best scores for J28 run on July 28th. On July 29th the J28 has still the best RMSE evaluation, but the best MB is calculated for J26. A lower model underestimation is observed on July 29th for J26 simulation where the main precipitation pattern is simulated properly.

Nevertheless, the better performance of J26 in the map comparison with respect to J28 on July 29th is rather unexpected, as the J28 run misses the main precipitation pattern.

3.6.3 Sensitivity to initial conditions

The low QPF performances of the J28 run for the 29th July can be related to the role of the specific ERA-Interim initial conditions. In support of this initial conditions, the study of Ahasan and Khan (2013), which was initialized on the same day of J28, but with a NCEP reanalysis, produced a better rainfall distribution for July 29th (not shown). To test the sensitivity to initialization I perform a new run, initialized on 28th July 2010 at 00 UTC

with a different set of initial conditions. Instead of using the ERA-Interim fields, I run J26 for 48 hours till July 28th at 00 UTC. Then all the microphysical variables deriving from the WRF dynamics (namely cloud water, rainwater, snow, cloud ice and graupel) are set equal to zero: this provides a set of initial conditions comparable with those provided by ERA-Interim (the same required by the WRF preprocessor WPS for ERA-Interim initialization). In ERA-Interim I do not have humid variables (microphysical variables), so I have tested the importance of this aspect, initializing the WRF restarted run in the same way. This new set of initial conditions is fed into the model and WRF is run for another 48 hours. In this way, I run a novel J28 experiment, initialized with the (partial) output of the J26 run. As shown in Fig. 3.6 and Fig. 3.7, the results of the J28 restarted run (J28R) outperform the original J28 results: the main precipitation core is well modelled and none of the main precipitation structures is missed. The restarted run produces daily rainfall outputs which are similar to those of J26, providing a better estimate of the main precipitation patterns and positions. Since the only difference between J28 and J28R are the initial conditions, these result suggest that the initial conditions provided by ERA-Interim on 28th July at 00 UTC are mainly responsible for the poor results provided by J28 on the 29th.

To better understand the evolution of the J28 and J28R runs, I compare the surface temperature (Fig. 3.8) and moist transport (Fig. 3.9) at the initialization time (July 28th at 00 UTC) and 24 hours later (July 29th at 00 UTC), at the beginning of the most intense day of the event.

At each horizontal point (pixel), the moist transport is defined as the vertically-integrated total moisture transport $\mathbf{F}$, [kg (m s)$^{-1}$] given by the product of the water vapor mixing ratio q [kg kg^{-1}] and the horizontal wind speed $\mathbf{V}$ [m s^{-1}]

$$\mathbf{F} = \int_{z_{Surf}}^{z_{Top}} \rho \, \mathbf{f} \, dz \qquad \text{where } \mathbf{f} = q\mathbf{V}.$$

At 00 UTC the J28R run is identical by construction to the J26 frame. Twenty-four hours later, I find that J28R and J26 present very similar precipitation, as shown in Fig. 3.6. Surface temperature and moisture transport fields are also very similar, so I choose not to show the J26 run in the comparison of Fig. 3.8 and Fig. 3.9, to make the comparison clear and straightforward.

The pixel-by-pixel differences for the temperature field at 2 meters between the ERA-Interim initialization (J28) and the (partial) WRF initialization (J28R), show strong temperature anomalies (Fig. 3.8). On July 28th, the J28 field shows a positive bias of more than 3K in north-western Pakistan, near the Afghanistan border, and a negative bias eastwards (Fig. 3.8, panel a3). The warmer zone of the J28 run can create a stronger instability of the air masses, with a tendency to generate intense precipitation in the next 24 hours (on July 28th) and drier and colder atmospheric conditions on July 29th.

The moist transport reflects the temperature anomalies (Fig. 3.9). On July 28th, both initializations generated a moisture transport directed towards the orographic barrier, even if the transport of the J28 run is more concentrated (Fig. 3.9, panels a1 and a2). The J28R run presents broader region with large amount of moisture transport.

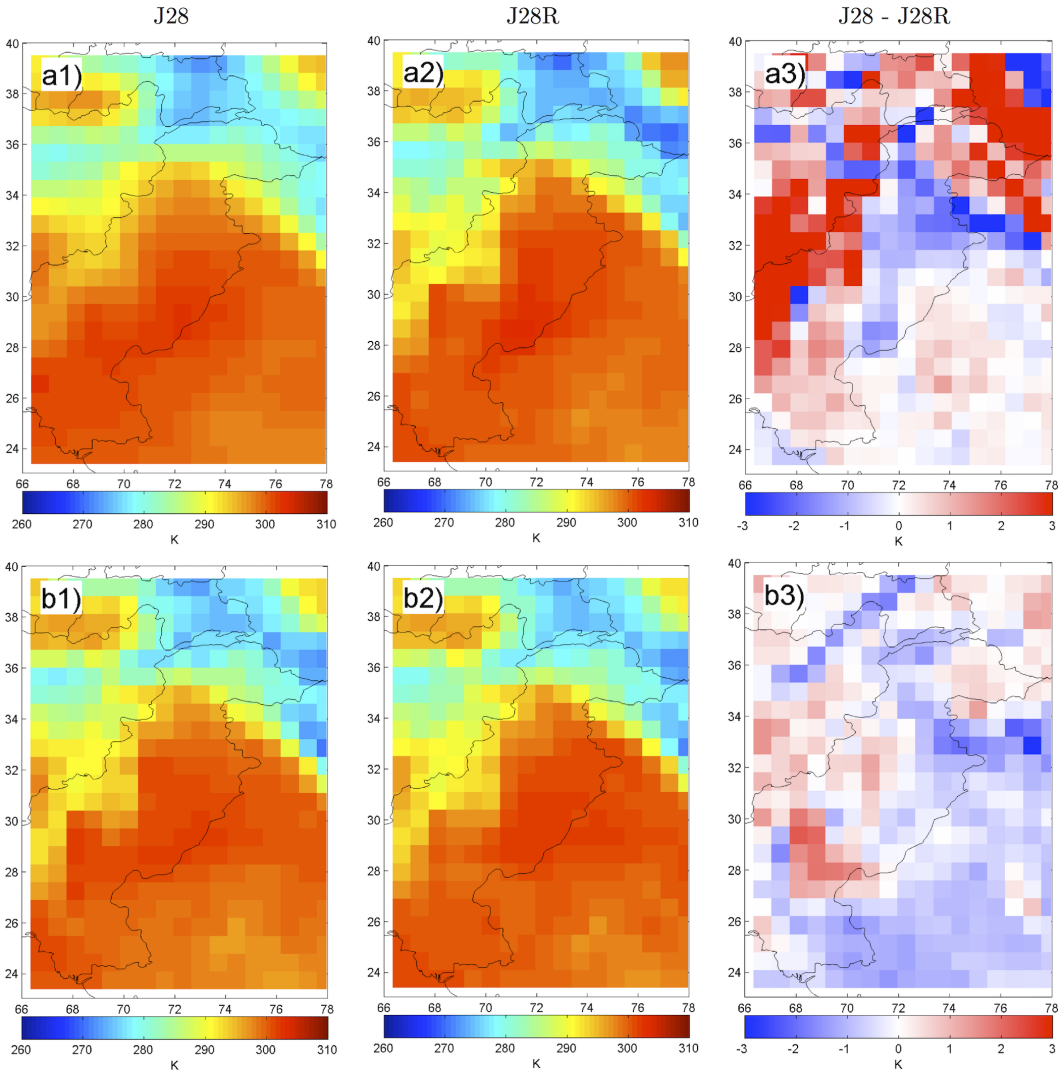

Figure 3.8: Surface temperature at the time of initialization (28th at 00 UTC) and on 29th at 00 UTC for the J28 and J28R runs. Upper row: Temperature field at 2m in the J28 run on July 28th at 00 UTC (a1); the same for the J28R run (a2); pixel-by-pixel difference between these two temperature fields (a3). Bottom row: Temperature field at 2m for the J28 run on July 29th at 00 UTC (b1); the same for the J28R run (b2); pixel-by-pixel difference between these two temperature fields (b3). Temperature fields are plotted at 0.75° horizontal resolution.

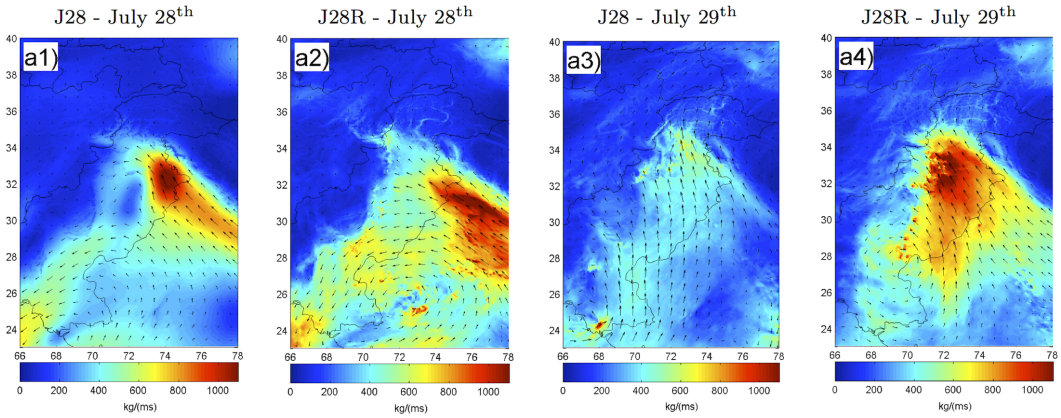

Figure 3.9: Moisture transport field for the J28 run on July 28th at 00 UTC (a1); the same for the J28R run (a2); moisture transport for the J28 run on July 29th at 00 UTC (a3); the same for the J28R run (a4). Moisture transport fields are plotted at the resolution of WRF simulations (3.5 km). The colors indicate the intensity and the vectors rapresent the directions of the moist transport.

The separate contribution of moisture fields and wind fields to total moist transport has been investigated in terms of horizontal and vertical distributions (not shown). The major contribution of the moisture flow to total moist transport is always more evident in the south west part of the domain, for both runs and days of the event. On the contrary, a predominant role of wind is apparent in the north east part of the study area, over the mountain region. Along the vertical, the highest moist transport occurs on lower levels, with a major contribution provided by water vapor, instead of wind (which contributes more significantly on higher levels).

On July 28th, the higher temperatures and the more intense transport are responsible for larger QPF exhibited by J28 run. The day after (Fig. 3.9, panels a3 and a4), the J28 run has completely lost the moisture transport contribution, while transport remains high for J28R. In the J28 run there is no moist convergence on July 29th (Fig. 3.9, panel a3), while in J28R the moist air is pushed towards the northern Pakistan orographic barrier producing heavy rain (Fig. 3.9, panel a4). All these factors concurred to create a more intense rainfall spell on the July 28th and a drier environment for the following day in the J28 run.

3.7 Qualitative and quantitative analysis of the vertical structure

Comparison of the surface precipitation patterns against TRMM has allowed to assess the overall performance of WRF for hydrological purposes. The comparison between the simulated CloudSat and CloudSat observations provides more insight into the ability of WRF to reproduce vertical profiles of cloud structure.

On July 28th at 21:00 (granule 22608) CloudSat passed directly over the system of interest. A comparison of simulated CloudSat using various assumptions and WRF experiments is shown in Figure 3.10. As a reference, the CloudSat L2B-GEOPROF is provided in the top panel (Fig.3.10, panel a). This graphs shows the surface clutter, when it is not attenuated by heavy precipitation above it like around 33°N.

It is evident that the changes in parameterizations and initial conditions result in major differences. These need to be interpreted in light of the temporal and spatial evolution of the system. Therefore I identify three salient features at the large scale (Fig. 3.10, panel i) and discuss how each experiment performed in that regard. First, the region of greatest hydrological importance in this portion of this event is the wide and persistent stratiform precipitation area between 33°and 35°N, which was for the most part generated by a relatively low convective plume (minimum IR brightness temperatures observed around 230 K) and advected moisture from the SE (hereinafter STR34N). Second, consider the organized convective towers along the southern part of the line of convergence, characterized by an anvil much less developed than what observed and top heights of the large hydrometeors (marking convective cores) barely reaching above 10 km, with corresponding IR in the 190 to 200K range (hereinafter CONV30N). It is important to note that at the time of the overpass, the line of convective activity curved to the SW around 29°N along the CloudSat ground track (blue line in Fig. 3.4 panel a6 and Fig. 3.6 panel a7), and therefore all convection occurring between 27°N and 29°N is not observed by CloudSat because it was to the west of the track. Such misplacement is noted here just to address a key feature, viz. the limited representativeness of nadir curtains when interpreting Figure 3.10: one should not conclude that a configuration did or did not produce convection according to observations only focusing on these data. The Geostationary imagery should always be consulted when interpreting these observations to provide the context that is lacking from the nadir-only profiles. All considerations expressed hereinafter were always developed in this context. The third feature considered is the long outflow associated with STR34N over the Karakoram range and the Taklimakan desert (latitude from 33°N to 35 °N) resulting for the most part in snowfall to the surface, but with the zero isotherm in close proximity to the prevailing ground altitude of the desert.

Panel b shows that the Exp-WSM6 experiment, initialized on J24, essentially failed to generate precipitation between 33°N and 35°N, as also shown in Figure 3.6. The CONV30N structure was much suppressed and disorganized, however a remnant plume did produce snowfall over Karakoram, albeit with cloud top heights 3 km lower than observed. Panel c shows the product of the same configuration but initialized on J26: in this case all three elements are captured to some extent, however the stratiform region is spatially much less extensive, the convective region extends more to the north, and most importantly exhibits notably deeper towers than observed (topping at 15-16 km). This comparison confirms that this configuration, while it achieved among the best statistical scores in total precipitation patterns, doesn't necessarily capture a realistic partitioning in convective vs. stratiform precipitation.

In order to assess the sensitivity of the forward simulations to assumptions inde-

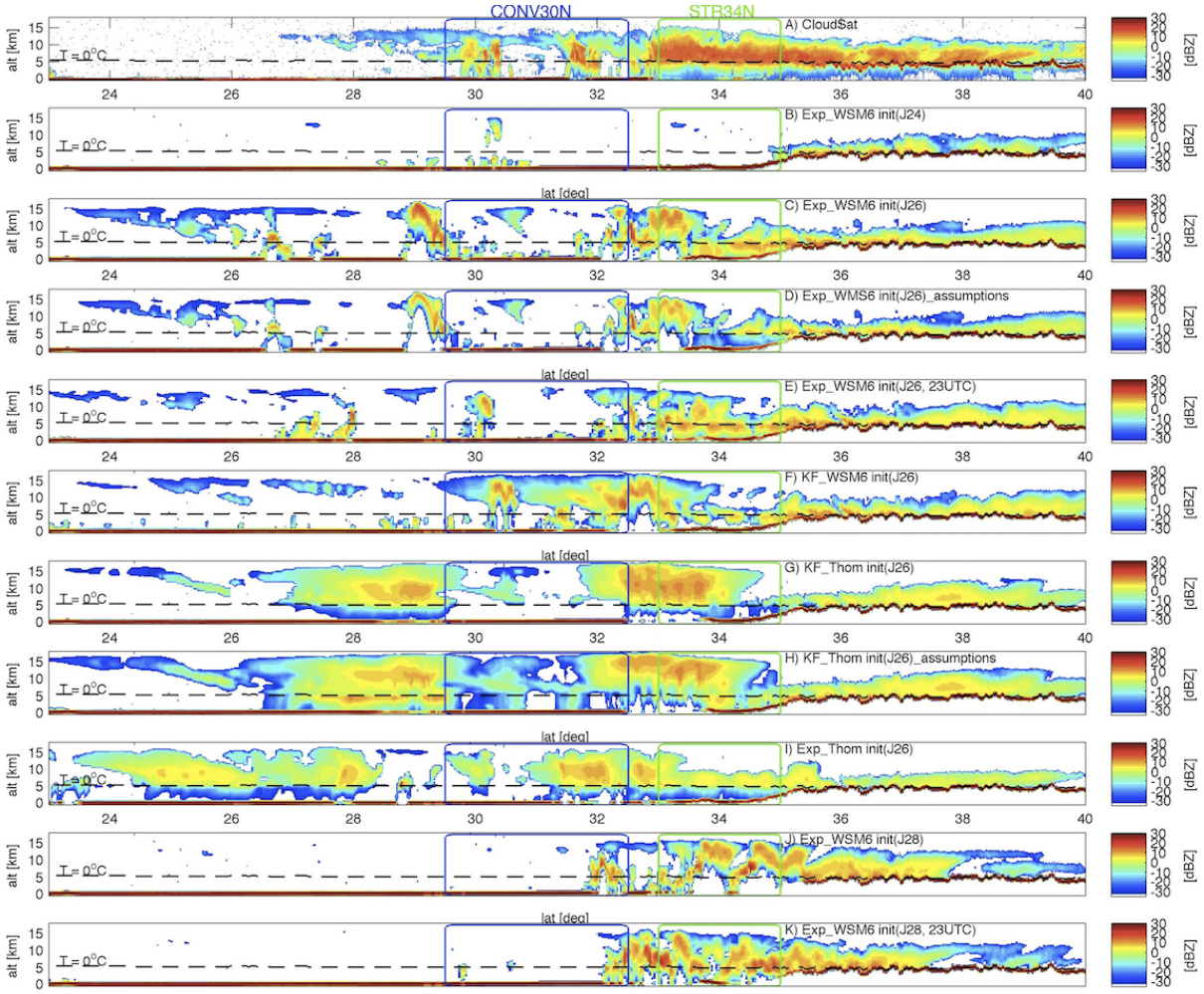

Figure 3.10: Vertical structure of the atmosphere on July 28th at 21 UTC. From the upper to the lower panel: CloudSat observation (Granule 22608) (a) and DS3 CloudSat simulations for Exp-WSM6 initialized on J24 (b), Exp-WSM6 initialized on J26 (c), Exp-WSM6 initialized on J26 with different microphysical assumptions (d), Exp-WSM6 at 23 UTC initialized on J26 (e), KF-WSM6 initialized on J26 (f), KF-Thompson initialized on J26 (g), KF-Thompson initialized on J26 with different microphysical assumptions (h), Exp-Thompson initialized on J26 (i), Exp-WSM6 initialized on J28 (j), Exp-WSM6 at 23 UTC initialized on J28 (k).

pendent of the bulk-hydrometeor quantities produced by these single-moment schemes, a series of tests using the same WRF output as input to the CloudSat simulation are performed: the assumptions on particle size distribution (PSD) and mass-size (m-D) relationship for the hydrometeor species are swapped between those assumed internally in the WSM6 scheme and those assumed in the Thompson scheme, plus a third set adopted in airborne precipitation radar microphysical retrievals. In each case the entire set of micropysical assumptions was swapped, and for all of them T-Matrix calculations (Mishchenko and Travis, 1998) were used to calculate the scattering properties of the hydrometeor species according to the internal assumptions within each module. Oblate spheroids were adopted for raindrops (Beard and Chuang, 1987) and snowflakes (Matrosov et al., 2008), and spheres for all other particles.

One example of these tests is shown in panel d (where both the PSD and m-D assumptions of Thompson are applied to the bulk quantities generated by Exp-WSM6 J26). Visual comparison of panels c and d confirms the intuition that at the level of assessment of the general aspect of cloud and precipitation systems, the microphysical assumptions made during the radar simulations are of second-order importance compared to the microphysical assumptions made in the CRM simulations. While the microphysical assumptions at the radar simulation stage change by several dB the observed reflectivities on various portions of the profile, but such change is indeed not sufficient to alter the visual interpretation of the general aspect of the systems other than in a small minority of locations. For example the only striking difference can be noticed in the rain portion between 33N and 35N where the Thompson microphysical assumptions generate reflectivities lower than the WSM6 by more than 10 dB. This particular difference is due to the fact that for low water contents WSM6 still assumes raindrops of about 1 mm on average, while the Thompson parameterization results in drop sizes smaller than 0.5 mm (notably, this change was explicitly targeted in that module to better reproduce mid-latitude light precipitation and drizzle, Thompson et al. (2008)). Therefore at W band, although the water content is identical (because it comes from the same WRF run), the 0.5 mm particle will be in a Rayleigh scattering regime, unlike the 1 mm, which in turns explains the large differences observed in the radar returns. Overall, an investigation focusing on quantitative retrievals of precipitation must indeed account for them, and the uncertainties within, but when CloudSat data are only used to validate the structure of the observed systems assumptions on PSD and scattering models, they become of secondary importance. These tests – performed on each one of the WRF experiments – served to eliminate one possible source of ambiguity in the interpretation of the simulated results. Along the same lines, I note that the DS3 simulator has a relatively basic representation of multiple scattering effects, particularly when compared to the advanced simulator DOMUS (Battaglia and Tanelli (2011)), which is included in NEOS^3. Nonetheless, it was found that the DS3 simulations yielded a more direct interpretation in regards to the nature of the problem. Absence of multiple-scattering effects is for example evident in the deep convective storm modeled at 29N in this simulation where the single-scattering signal is completely attenuated instead of showing the typical stretched echo of multiple scattering all the way to the surface and beyond (see Battaglia

et al. (2010) for a comprehensive review on multiple-scattering).

Panel f shows the product of the KF-WSM6 J26 experiment. Despite identical synoptic conditions and microphysical parameterization, this experiment generates much more developed anvils around CONV30N. However it fails to capture the stratiform region of greatest interest (STR34N). The low statistical scores quantify the fact that this experiment overestimated precipitation in CONV30N and underestimated it in STR34N. Panels g and h show the products of KF-Thompson J26 with Thompson and WSM6 assumptions in the radar simulations, respectively. The higher propensity of this microphysical parameterization to produce anvils and resulting stratiform rain is manifest in both cases. The Thompson scheme, unlike a simple single moment scheme, explicitly predicts the mixing ratio and the number concentration of cloud ice (Thompson et al., 2008). In this scheme the rain size distribution significantly shifts depending on whether the rain appears to originate from melted ice versus rain produced by collision/coalescence (warm rain). As evident from Fig. 3.10 (panels g,h,i), the largest reflectivity factors are usually observed above the line of melting level and the volume above this level is significantly enhanced in the Thompson scheme simulations. Consequently, it generates convection even deeper than WSM6, and produces wider anvils. The latter aspect is more in line with observations, but combined with the former it results in an overestimation with respect to TRMM products (Fig. 3.5).

Comparison to the CloudSat reflectivities in the rain portion shows much smaller values in the model than in the observation: this is likely due to the aforementioned assumption of small raindrops in Thompson and the absence of significant multiple-scattering contribution in the simulation. Small drops result in unattenuated reflectivities that are possibly biased low, and if the water contents are overestimated the specific attenuation can be larger than observations (it is almost independent on drop size), these two factors, combined with the absence of multiple-scattering stretched echo generated in the ice region above, provide a framework to explain this particular difference. Notably the model runs used to generate these simulated CloudSat products apparently extend the region with precipitation more southward than observations. This is because the line of convergence mentioned before did not bend SW at 29 °N as in reality, once again reflecting the great importance of the choice of microphysical parameterizations not only in the resulting storm structures, but also in the large scale patterns.

Panel j shows the product of Exp-WSM6 J28. In this experiment the entire set of features is moved northward, the region of highest accumulation on July 28th is captured better than the other cases, but not because of an improved skill in capturing the nature of the process (which is entirely convective at this time with no significant anvil).

Finally, a perturbation analysis was applied to the simulations to examine the importance of shifting the simulated track relative the core of the precipitation and the importance of the timing of the WRF run. This is particularly relevant when studying convection, for which location and timing of occurrence are fundamental. To this end, I looked at the satellite simulated overpasses shifted by 0.8 °to the East/West with respect to the center of the main precipitation core and using hourly WRF runs in a range of plus and minus three hours about 21 UTC (time range comparable with the time evo-

lution of these cloud structures). To serve as a reference, the actual CloudSat overpass was also overlaid on a map of IR temperature from Geostationary satellites. Perturbing the simulated tracks did not reveal any significant improvement and if anything led to sometimes missing the main core of the precipitation. For this reason, I focused on the nominal CloudSat track. Regarding the timing analysis, I have focused my investigations on J26 and J28 (Exp- WSM6) simulations. For each of these hourly simulations, the simulated radar products were compared to the CloudSat measurements in terms of their contour-frequency-by-altitude diagram (CFAD). Namely, I considered the a vector consisting of the vertical profiles of the 10%, 50% and 90% quantiles of the simulated CFADs and compared them to those of the CloudSat data. For instance, the correlation coefficient between the CFAD of CloudSat measurements and that of the simulated results at 21UTC is equal to 85% for J26 (Fig.3.10 panel c) and 93% for J28 (Fig.3.10 panel j). The strongest correlations to the measurements are observed with the WRF products at 23 UTC for both J26 and J28, with correlation coefficients of 96% in both cases. The corresponding resulting radar cross sections are depicted in Fig.3.10 (panels e and k) for the J26 ad J28 runs are 23 UTC. For the J26 case (Panel e), a comparison with the results at 21 UTC (panel c) shows that the clouds and precipitation have moved to the North, as evidenced by the convective cell around 30°N in the CONV30N region. Furthermore, similarly to the CloudSat measurements, the top of the cells is lower at 23 UTC than at 21 UTC, which explains the slightly larger correlation between CFADs. Nonetheless, there is still a strong resemblance between the features at both instants, e.g. in the STR34N region where the precipitation in still disorganized. Similar observations can be made for the Exp-WSM6 case initialized on J28 (panels j and k) where results at both times capture the persistent precipitation in the mountains (north of 35°N). One can note also the lesser impact of attenuation on the measurements at 23 UTC in the STR34N region (around 34°N) owing to the lower levels of the clouds at that time.

3.8 Summary and Conclusions

In this chapter I have performed WRF non-hydrostatic simulations at 3.5 km of the HIWE that led to the Pakistan flood in July 2010. I have tested the ability of the modelling system to reproduce the observed precipitation rates and patterns, and I have analyzed the model sensitivity to different microphysics and convection parameterizations and different initializations.

Explicit convection and the WMS6 microphysical scheme turned out to provide a better match in terms of rainfall amount, patterns and localization when compared to other choices.

Using this configuration, I varied the initialization day to determine the dependence of the model results on the choice of initial and boundary conditions. Even though model outputs are usually more reliable in the first days of the simulation, the J28 run (initalized on July 28$^{\text{th}}$) performed poorly on July 29$^{\text{th}}$, especially when compared to a run initialized on July 26$^{\text{th}}$. This uncommon behavior motivated an additional set of experiments. A new model run (J28R) was initialized on July 28$^{\text{th}}$ with the inputs

provided by a WRF simulation started on July 26th, with all variables related to clouds and vertical velocities set to zero to be consistent with a standard large scale inizialization. This novel run outperformed the original J28 run initialized with ERA-Interim fields, both in terms of rainfall localization and patterns, as well as of daily accumulation. The WRF run, starting two days before of the test day, may provide by itself, initial conditions more reliable than the ERA-Interim for the rainfall representation. This initial condition perturbation experiment give some insights on the simulation of complex events with limited initial condition characterization data.

This achieved results indicates that the initial conditions are a crucial factor in order to obtain a satisfying representation of the event.

The joint use of CloudSat observations and simulated cloud radar profiles allowed to investigate further the skill of each experiment in capturing the most important aspects of the observed vertical structure of this event. In this regard, the Thompson microphysics produces more stratiform precipitation and more organized precipitation patterns than the WSM6, in line with the observations. Both microphysical parameterizations produce convective activity deeper and more intense than observed. Since Thompson also produces more extensive widespread precipitation from the outflow, it results in an overestimation of the total precipitation. The striking differences in cloud structure resulting from the different microphysical and cumulus parameterizations, even when the same synoptic conditions are adopted, reinforce the assessment that performance of models in reproducing QPE estimated from observations cannot be limited to a few exercises with different models, resolutions or initial conditions. Notably, the principal differences resulting from the adoption of different parameterizations within a particular model (in this case WRF) are consequence of their resulting macroscopic distributions of the bulk quantities of the various hydrometeors and of the different latent heating profiles and they can radically change the final output of the model given equal initial conditions and resolutions.

Overall, I found that the simulation results are affected more significantly by the choice of the initialization day than by the parameterization schemes adopted. As expected, the largest errors are located near Himalayas and northern Pakistan, where the steep local orography affected the numerical integration.

All the study has dealt with the presence of the highest mountain topography of the world and the experiment of going to 3.5 kilometres resolution with a non-hydrostatic model has represented an instrument to understand the physical processes responsible of the tragic event. In particular I have found that ICs and BCs are a prominent factor affecting the results and that small variations in local atmospheric dynamics can produce very different results in complex orography areas. This study has investigated the event at different spatial and temporal scales, starting from the large scales, down to the mesoscale fields (section 5b and 5c) and vertical sections (section 6). The synoptic features of the different initializations in terms of geopotential, temperature and water vapor mixing ratio are pretty similar for all the runs and the WRF successfully reproduces the main large scale features responsible of the event. Moreover, the model, as expected, strongly reflects the large scale characteristics inherited by the coarsely resolved GCM.

The highest differences are evident when the model is challenged to reproduce the smaller scale features. The different pattern results obtained for J26 and J28 run are a manifestation of this: the presence of a valley or of a ridge is capable of strongly influencing the simulation, producing different moisture transport and wind circulation that affect the resulting precipitation fields. As stated in Webster et al. (2011), the predictability of this event was evident from large scale models, but I agree with Rasmussen et al. (2014) that conclude that an higher degree of detail is needed to understand the anomalous convective features that led to the tragic flooding.

This work focuses on a specific extreme event, viz. the 2010 Pakistan flood, studied using the WRF model in cloud permitting mode and operated at 3.5 km in order to gain insight on the predictability of this flood event. While in general it can be difficult to make solid conclusions on the choice of any one or the other microphysics from individual case studies, nonetheless the results allow to draw some more general conclusions. In particular, they suggest that a careful choice of parameterization schemes and initialization day must always be adopted, because these factors can affect significantly the simulation. Configurations that at the large scale exhibit small differences, at the small scale start to produce very different precipitation amounts, patterns and circulations, especially over mountain terrain. The results presented here indicate that the reliability of the large scale fields used for initialization and boundary conditions remains an essential ingredient of the simulation, and that errors in the large scale fields can be propagated, or even amplified, in the outputs of high-resolution simulations. For all these reasons, I recommend a dual selection of both initial and boundary conditions and parameterization assumptions to propagate the model through this kind of events in complex topography areas, rather than an independent analysis of one or another. Inter-scales phenomena and orography interaction are thus predominant features in studying these particular processes over complex orography areas such HKKH.

This study intends to contribute to future studies in that area, and it highlights the complexity of studying an HIWE case study in a geographical area in which the ability of numerical weather models is seriously challenged. A follow on project consist in analyzing the impacts of the Pakistan flood, attaching a WRF-Hydro simulation to the present WRF stand-alone experiment.

Chapter 4

WRF and WRF-Hydro fully coupled experiment: application over the Tiber river basin in central Italy

4.1 Introduction

As stated in the previous chapters, the main aim of this study is to compare the classical WRF stand alone meteorological approach with a fully coupled WRF/WRF-Hydro configuration in order to evaluate the eventual contributions of the atmospheric feedbacks in terms of precipitation predictability.

The classical meteorological approach requires the use of a numerical weather prediction model (in my case WRF) and a land surface model (Noah-MP in my experiment) to reproduce the main features of the atmospheric processes and their interaction with the surface. In the fully coupled hydro-meteorological modelling I am adding a distributed hydrological model (the WRF-Hydro model suite) to introduce additional physical processes in the modelling system that contributions to the redistribution of the water at the surface on an high resolution DEM-based grid by means of routing processes (surface, subsurface, baseflow, lake and reservoir storage - for further informations see chapter 2), that permits to the water to infiltrate and exfiltrate during its way toward the channels (Fig. 4.1).

In the coupled approach, for every time step of the atmospheric model, the meteorological variables are passed from the WRF model to the LSM and the fluxes are partitioned towards the surface. Then, the routing is calculated over the high resolution grid, and the update surface states in terms of soil moisture and water partitioning at the surface are reaggregated and given back to next time step of the WRF model by the LSM. At the contrary, in a WRF stand alone simulation all the surface processes are represented by the 1-D LSM column-model for every pixel in the domain and every time step. In addition to that, a fully coupled experiment provides not only outputs in terms of atmospheric variables, but also distributed hydrological fields such as streamflow informations in the channel network, soil moisture and snowpack distributed fields.

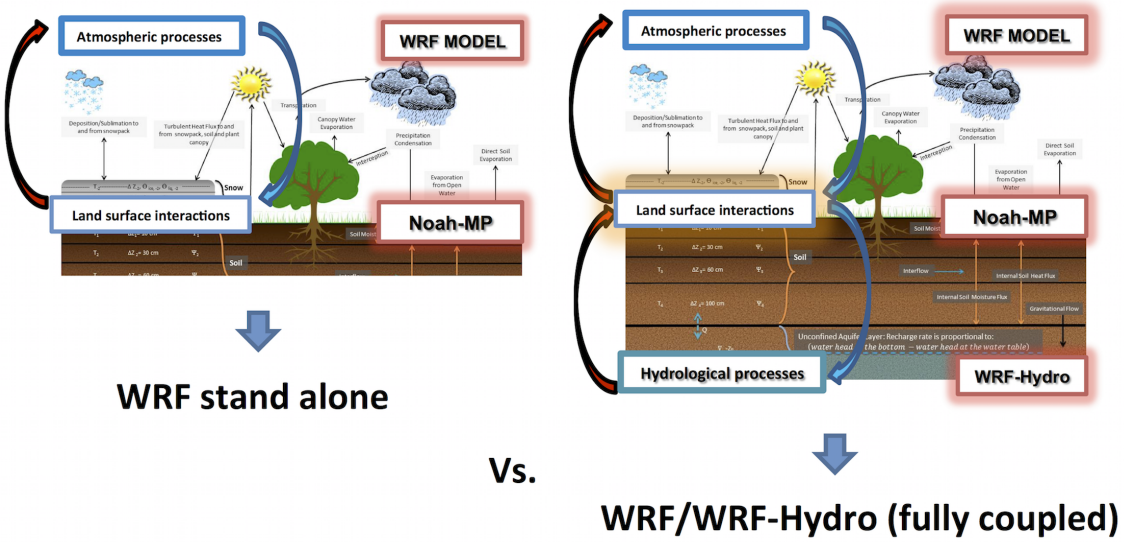

Figure 4.1: Simple schematization of the experiment. Adapted from figure from Noah-MP website (http://www.jsg.utexas.edu/noah-mp/)

The studies of Givati et al. (2016), Senatore et al. (2015) have compared the one-way implementation of the WRF-Hydro system to the WRF/WRF-Hydro fully coupled approach in the Mediterranean region, in Ayalon basin in Israel and in the Crati catchment in Southern Italy respectively (see section 2.5 for more informations and references). All of these studies have highlighted the potential of a two-way atmospheric-hydrological coupling in improving hydro-meteorological forecast both in early flood warning applications, water resources management and the high demand of further research in this kind of land-atmosphere coupling mechanisms. According to some event-based preliminary studies at the beginning of the PhD project and according to Senatore et al. (2015), at the event scale not sensible differences are experienced in terms of surface runoff redistribution on the fully-coupled approach, especially for synoptically driven kind of events, where the main moisture contribution comes from the large scale transport, instead of land-atmosphere moist and heat fluxes. For these reasons I have moved towards longer time scales, expecting higher influence of water redistribution at the surface, infiltration and exfiltration hydrological processes at the seasonal scale, especially during dry season where the contribution of fluxes is more relevant to the formation of locally driven summer convective storms. In my study the two model approaches (stand-alone WRF vs. fully coupled WRF/WRF-Hydro) are explored over one year of simulations (2012) and at high resolution in complex topography area in the Mediterranean region. In this framework, a key question is "Does the soil-atmosphere feedback add a significant contribution in the reproduction of soil moisture and in the storm-runoff generation?". In particular, I want to investigate the capability of WRF vs. WRF/WRF-Hydro model suite to describe the physical processes leading to severe rainfall in complex topography areas and

the sensitivity of each model configuration to the choice of different parameterizations. In this contest, a correct model calibration for both atmospheric and hydrological needs is crucial. The two WRF and WRF-Hydro model suites deals with different aspects of meteorological and hydrological processes, crossing a wide range of spatial and temporal scales. For these reasons, choosing an appropriate model setting both for atmospheric processes and surface hydrology became crucial when the two models are used in coupled configuration (section 4.2.1). It is not possible to proceed to the coupling experiment, if a proper WRF model setting and a WRF-Hydro calibration is not selected in order to realistically represent the typical meteorological and hydrological processes happening in the region of study.

In this chapter I have started from the classical meteorological approach (the same method used also in the Pakistan experiment) and I have performed four different WRF one-year-long stand alone simulations over central Italy (Kain-Fritsch and explicit cumulous parameterization/Thompson and WSM6 microphysics) (section 4.3). In a second step, I calibrate the WRF-Hydro distributed model and the main Noah-MP LSM parameters with a forcing as close as possible to reality (called hereinafter "perfect forcing"), derived from observations and analysis data instead of WRF model variables. In addition to that, I update the default USGS land cover information of WRF with the most updated CORINE land cover dataset (last update in 2012, see Büttner (2014)), in order to provide the most state of the art conditions to the hydrological simulation (section 4.4). When both the atmospheric and the hydrological models settings are chosen and validated, then I can apply these settings to WRF and WRF/WRF-Hydro fully-coupled comparison and move forward the final results discussion (described in section 4.6). In this last step, I analyze the main rainfall-runoff controlling variables to investigate the possible improvement in predictability if I compare WRF stand alone and WRF-Hydro model applications, to understand whether it is more relevant going to higher resolutions and, in general, having a better description of the dynamics (correct choice of parameterizations etc.) or a better representation of the physical processes (meteorological only approach Vs. fully coupled hydro-meteorological WRF-Hydro simulations) in the representation of some kind of extreme hydrometeorological events.

I have performed this experiment over the Tiber river basin, one of the most important catchments in central Italy (section 4.2). Even if the topography is not as complex as the HKKH (chapter 3 experiment), the Tiber river basin is characterized by the presence of the Appennine mountain range for most of its basin area extension and elevations ranging to 2500 m above sea level. An additional advantage of performing the comparison of WRF and WRF/WRF-Hydro fully coupled experiment over this area is derived from the dense observation network available over the area (meteorological stations, soil moisture measures and fluxes stations) (section 4.2.2). Finally, since most of the WRF-Hydro studies has been developed in the Mediterranean area (Givati et al. (2016), Senatore et al. (2015), Yucel et al. (2015)), the Tiber river basin experiment is intended to provide another additional testbed to the hydrometeorological coupling studies performed in this climate sensitive area of the world.